III.D. FOURIER IMAGE PROCESSING TECHNIQUES

III.D.1. Optical Diffraction

Optical diffraction is arguably the simplest Fourier image processing technique, and is often the first processing step in studies where the primary data are images recorded on photographic film. The main advantage of optical diffraction is that it provides an objective way to assess and reveal periodic structural information in images. Klug and Berger (1964) were the first to use an optical bench to examine and record diffraction patterns from electron micrographs and thereby objectively analyze structural information in images of biological specimens.

a. Forming the diffraction pattern

Optical diffraction patterns are easily produced from selected (masked) regions of micrographs. A simple optical bench consists of a laser, which is used to produce a parallel, monochromatic beam that illuminates a specific area of the micrograph, and a (diffraction) lens to focus the Fraunhofer diffraction pattern in the back focal plane of the lens. The pattern may be viewed directly, but with due caution to avoid focusing the bright, central spot formed from the unscattered rays on the retina. The pattern is also often recorded on a standard photographic emulsion.

b. Experimental apparatus: the optical diffractometer

There are numerous diffractometer designs. They are generally categorized into one of two basic classes depending on whether the optical path is straight (**linear diffractometer**: Fig. III.60) or bent by use of optically flat mirrors (**folded diffractometer**: Figs. III.61 and 62). The type of diffractometer one chooses to use depends, in part, on the intended use of the apparatus. The folded design is usually preferred for rapid screening of a large number of micrographs when image quality and specimen preservation need to be assessed in order to select images for subsequent optical (§ III.D.2) or digital (§ III.D.3) filtering operations. For high quality optical reconstruction work (§ III.D.2), the linear design is generally preferred since there are fewer optical components, and thus fewer aberrations.

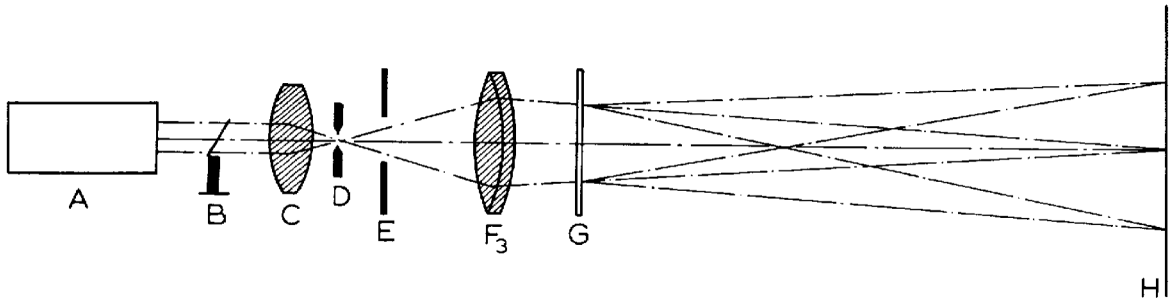

Fig. III.60. Simple, linear, optical diffractometer. The diagram shows the arrangement of the components used to construct a simple optical diffractometer. A. Laser; B, shutter; C, beam expanding lens; D, pinhole; E, adjustable diaphragm; F3, diffraction lens; G, electron micrograph; and H, viewing screen or camera. (From Horne and Markham, 1972, p.336)

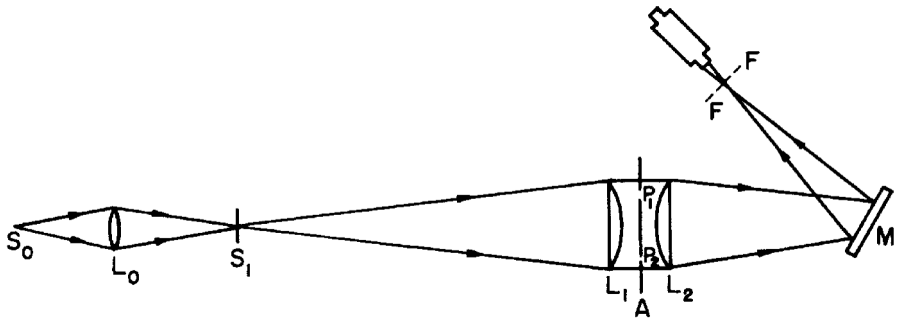

Fig. III.61. Schematic diagram of an optical diffractometer. (From Thompson, 1972, p.48)

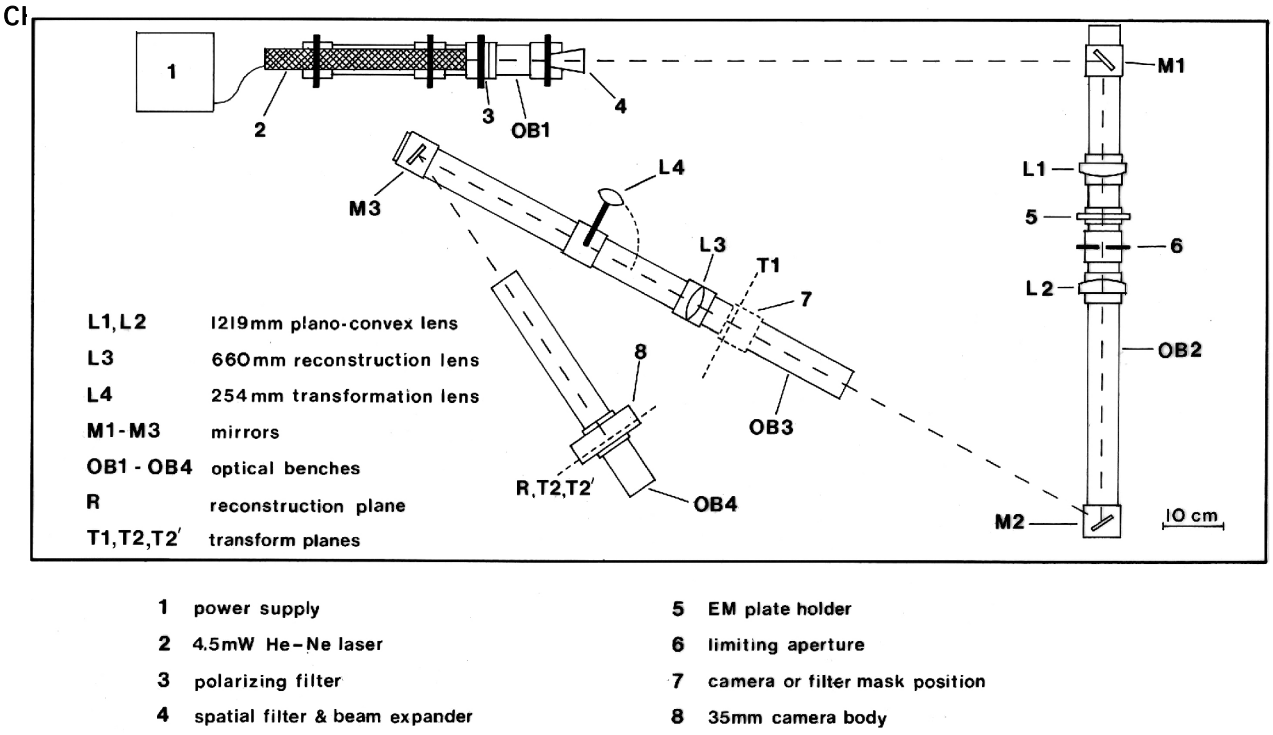

Fig. III.62. Diagram of the folded optical diffractometer, built at UCLA in 1972.

A diffractometer of reasonable quality, suitable for simple experiments such as screening images or detecting and locating periodicities, can be built or purchased for a few thousand dollars or less. More expensive designs ($10,000 or more) are usually easier to use and align, and produce high quality diffraction patterns and reconstruction images. A high quality diffractometer usually includes an image reconstruction system (with a high-quality, corrected, doublet lens), a pinhole spatial filtering system to remove noise in the illumination beam, a moderate-to-high power laser (1-50 mWatt), high-quality, high-reflectance mirrors (if the optical path is folded), fully adjustable, precision holders for all components, and an image and diffraction pattern recording system.

Many laboratories prefer to construct their own diffractometer with specifications dictated by the intended use of the instrument. For example, if most of the image reconstruction work is to be performed on a computer, a simple and inexpensive linear diffractometer for surveying images will suffice. The use of liquid gates, in which micrographs are submerged in oil to iron out in homogeneities in the micrograph emulsion (and glass or gelatin backing), produce diffraction patterns in which Friedel symmetry is nearly perfectly preserved (Table 1.I.C.2.e, Baker, 1981). However, such extreme measures prove to be inconvenient in practice and, in any event, present day digital processing systems are both fast and reliable and are usually preferred over high-quality optical processing systems.

Details of the design, operation, components, alignment, and calibration of optical diffractometers can be found in several references (Horne and Markham, 1972; Mulvey, 1973; Johansen, 1975; Erickson, *et al.*, 1978; Baker, 1981). The optical diffractometer, much like the electron microscope, needs to be carefully aligned and calibrated to perform optimally.

c. Applications of optical diffraction

Optical diffraction provides useful information about the geometrical arrangement of subunits in the specimen. Such structural detail often cannot be discerned by simple, visual inspection of the original micrograph. For example, the presence of rotational screw axes or pseudo-symmetries may go undetected without the information provided by the optical diffraction pattern. These types of structural information are determined by correctly indexing the pattern, that is, defining a lattice (or lattices for multilayered or helical particles) that accurately defines the location of all diffraction spots.

Indexing is an essential step for correct application of optical or digital filtering, or for many 3D reconstruction techniques (§ III.D.2). Except for some helical and multilayered particles, the

indexing of OD patterns from most planar specimens is quite straightforward. Articles by Finch, Klug and Nermut (1967), Moody (1967), Kiselev and Klug (1969), DeRosier and Klug (1972), Lake (1972), Leonard, Kleindschmidt and Lake (1973), and Unwin and Taddei (1977) give excellent examples of how pattern indexing is performed (these and additional examples are cited in Table 1.I.D.8, Baker, 1981). Misell's book (1978; pp.106-122) devotes an entire section to theoretical and practical problems of indexing. Artifacts in optical diffraction patterns sometimes make indexing difficult (Table 1.I.E, Baker, 1981). The characteristic, prominent "cross" observed in many optical diffraction patterns is mainly a consequence of strong diffraction caused by the edges of the mask used to select a region of interest in the micrograph. This feature is regarded as "noise" in the pattern and thus, should not influence the selection of a consistent indexing scheme. A typical example of an optical diffraction pattern recorded from an image of a negatively stained 2D crystal of catalase is shown in Fig. III.63.

Several applications of optical diffraction include:

- Accurate measurement of lattice parameters (unit cell dimensions) (Fig. III.63)
- Detection of rotational and translational symmetry elements (Fig. III.63)
- Determine relative orientation of multilayered specimens (*e.g.* stacked 2D sheets or opposite sides of two-sided structures)
- Detect and measure specimen preservation (distortions, overall resolution, radiation damage) for selecting best images for further image analysis
- Assess short/long range order in periodic specimens (Fig. III.64)
- Identification of signal vs. noise in images (Fig. III.63)
- Ability to examine specific small areas (Figs. III.63, 65-67)
- Determine electron optical conditions, *i.e.* contrast transfer function (focus, drift, astigmatism, etc.) at time micrograph was recorded (Figs. III.63, 65-67)
- Determine the hand of 3D structures (from metal-shadowed or tilted specimens)
- Superb device for teaching principles of diffraction, symmetry, and Fourier transforms

Optical diffraction techniques have been successfully employed in fields outside electron microscopy, for example, in the study of small-molecule crystal structures. In fact, pioneers of X-

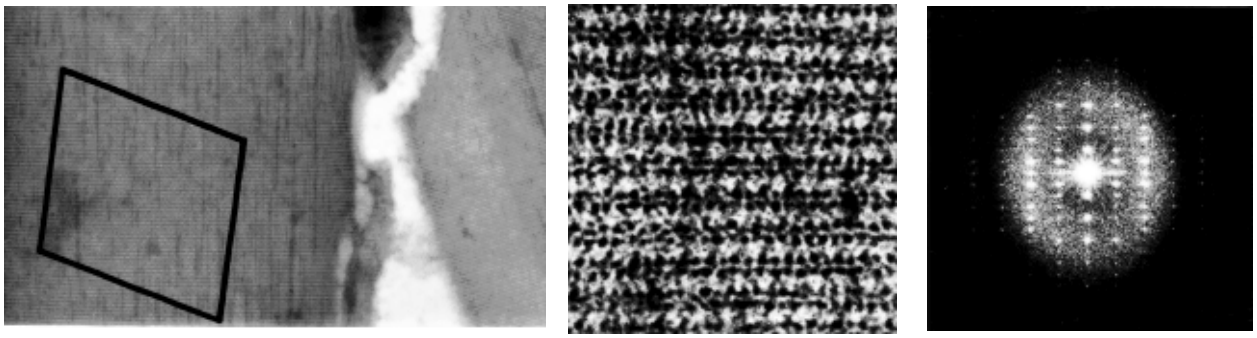

Fig. III.63. (Left) Low magnification micrograph of negatively stained bovine liver catalase. (Right) High magnification view of small portion of same crystal. (Right) Optical diffraction pattern recorded from the area outlined in the low magnification image.

ray crystallography were responsible for much of the original development of diffractometers. W. L. Bragg (1939) designed the first optical diffractometer, calling it a "new type of X-ray microscope". Several crystallographers used optical diffraction methods as an aid in solving small molecule crystal structures. By comparing diffraction patterns produced by models of the crystal structure (using various size holes punched in sheets of metal at predicted positions to represent atoms) with the experimentally recorded X-ray diffraction patterns, it was often possible to rule out incorrect structures and thereby verify or solve a crystal structure.

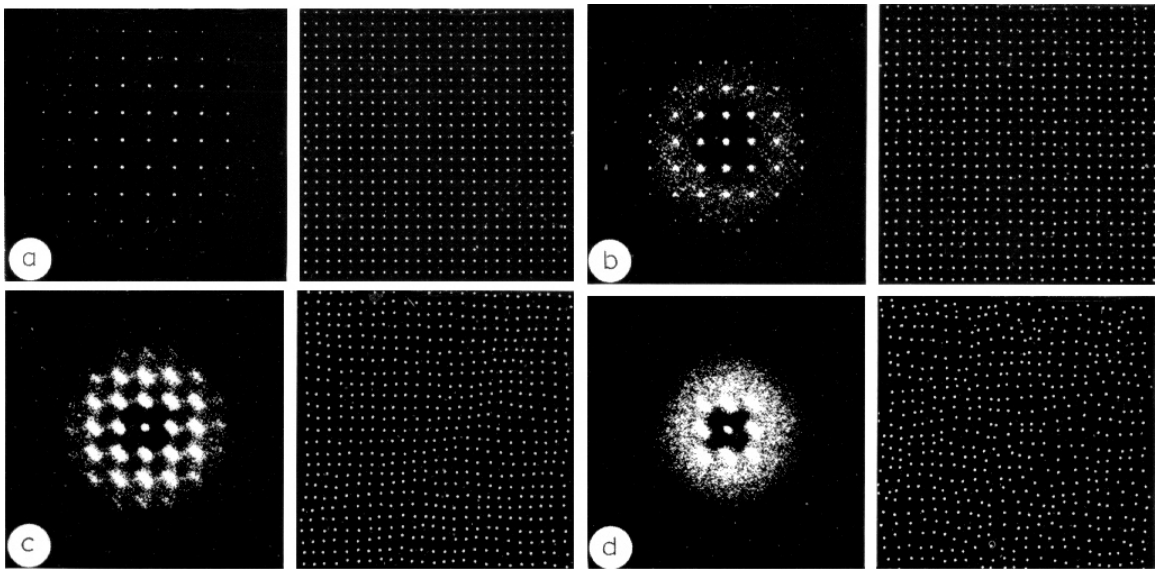

Fig. III.64. The effect of lattice disorder on the diffraction pattern. (a) Ordered lattice. (b) Vertical disorder of ±10%. (c) Two-dimensional disorder of ±10%. (d) Two-dimensional disorder of ±25%. (From Misell, 1978, p.72)

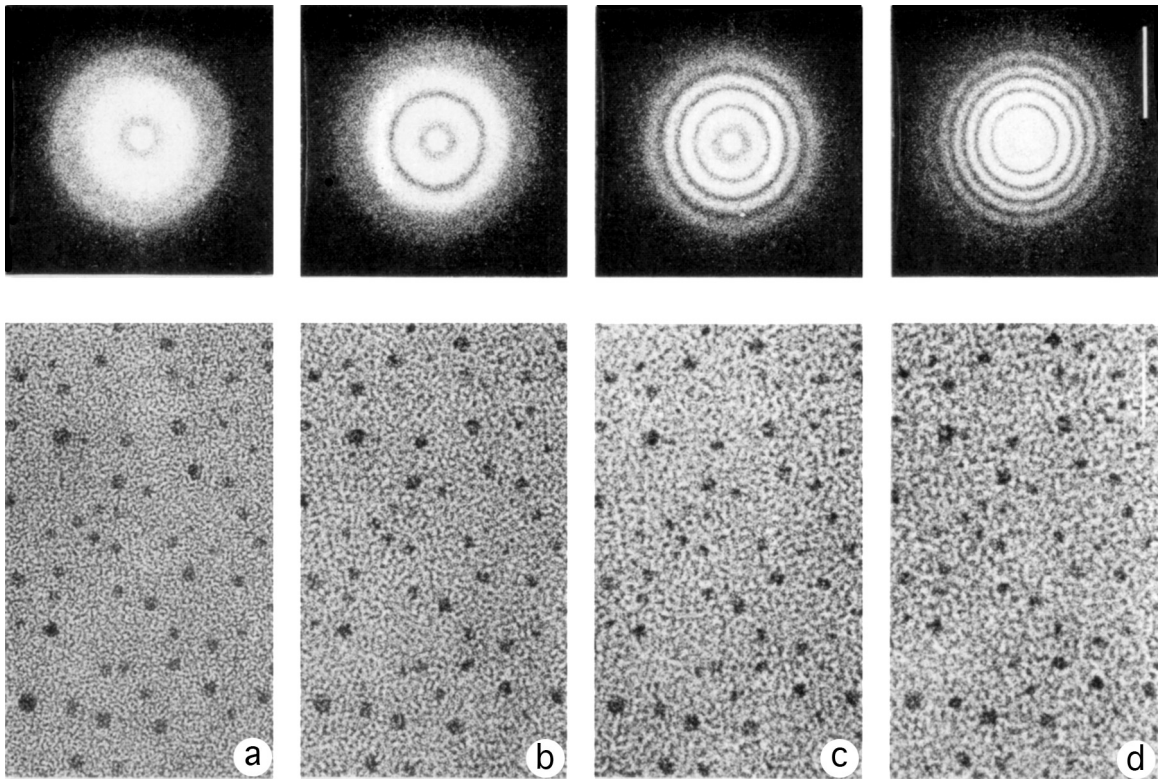

Fig. III.65. Focus series of thin carbon film. The black dots are gold atoms added to assist in focusing. The optical diffraction patterns above each image indicate (a) optimum defocus, (b) 150-nm under focus, (c) 210-nm under focus, (d) 250-nm under focus. Image bar = 10nm. Diffraction bar = 3.0 nm^{-1}. (From Misell, 1978, p.60)

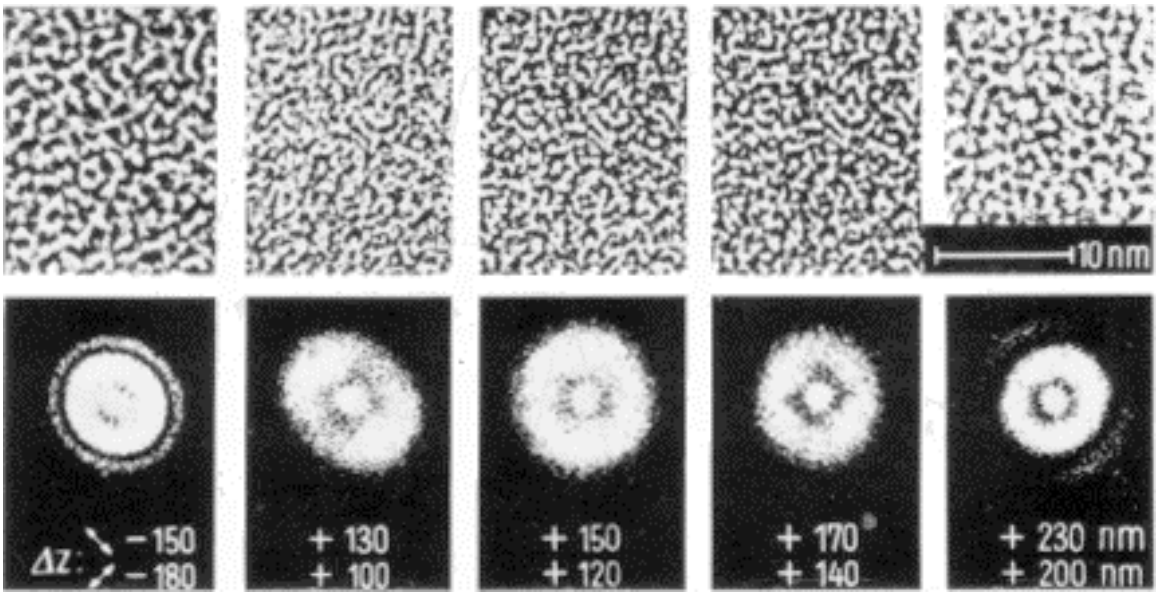

Fig. III.66. Micrographs and optical transforms of a carbon film, showing the effect of axial astigmatism and the determination of its direction. (From Misell, 1978, p.64)

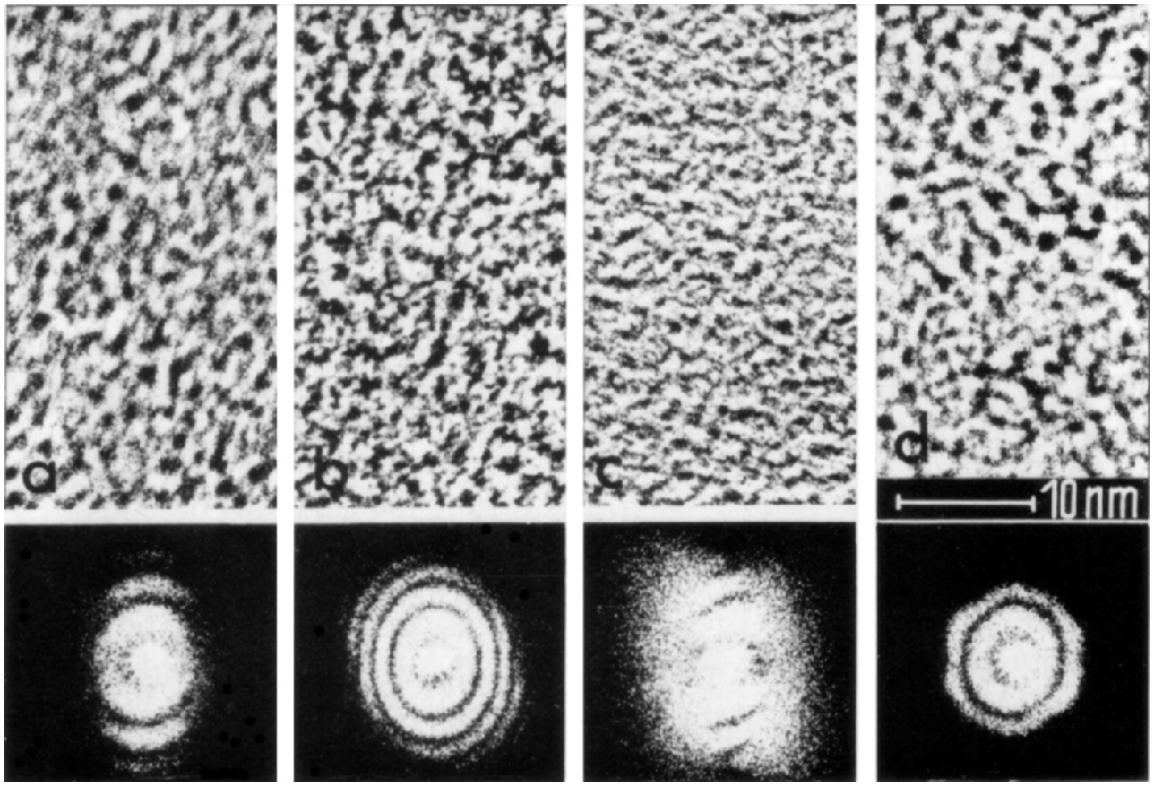

Fig. III.67. Images of a carbon film (top row) and corresponding optical transforms (bottom row), showing different image defects: (a) specimen drift, (b) miscentered objective aperture, (c and d) electrical charging of the objective aperture as a result of contamination, for example. (From Misell, 1978, p.65)

III.D.2. Optical Filtering

Klug and DeRosier (1966) and Bancroft, Hills and Markham (1967) independently introduced the use of optical filtering. This technique is mainly suitable for the study of periodic specimens with translational symmetry. Optical filtering provides a relatively straightforward way to remove the contributions from noise in micrographs and thereby reveal clearer images of specimen structure. In addition, it is a powerful method for separating Moiré images of multilayered specimens. Other applications are outlined Table 1.II.B of Baker (1981). Optical filtering is rarely (if ever) practiced these days and has been replaced by computer-based processing methods because they offer a number of significant advantages over optical processing (§ III.D.3). Nonetheless, a basic understanding of the method provides an excellent foundation for learning the principles that underlie Fourier-based image processing.

The review by Erickson, Voter, and Leonard (1978) and articles by Klug and DeRosier (1966) and Fraser and Millward (1970) give excellent introductions to the theory and practice of optical filtration. The basic principle of the technique is straightforward, but the method can easily lead to erroneous results especially for inexperienced researchers.

a. Indexing the diffraction pattern

The first, and most important step in an optical filtering experiment is to correctly index the optical diffraction pattern obtained from the specimen image. A pattern is considered successfully indexed if it is possible to distinguish between spots arising from noise (aperiodic image details) and those attributed to the periodic nature of the specimen. Although it is unnecessary to attempt to identify all the noise components in the unprocessed image, a correct filtration experiment requires knowledge of how noise and signal components are distinguished. For most crystalline specimens, the diffraction pattern is a lattice of bright spots (Bragg reflections) against a weaker background of noise (Figs. III.63, 68-69). Noise, or aperiodicity in the image, produces diffraction data of widely varying intensities in all parts of the pattern. Note that "periodic noise", i.e. noise located at or close to the lattice points of the diffraction pattern, **CANNOT be removed** by filtering. Systematic specimen flattening or staining artifacts are examples of situations that produce periodic-type noise. Other major sources of noise are listed in § III.B.

If the diffraction pattern proves to be difficult to index, an incorrect lattice may have been identified (*e.g.* because a super lattice has been missed). Occasionally, strong, non-indexible spots may be attributed to multiple scattering (Table 1.I.D.7, Baker, 1981) or they might arise from strong, aperiodic features in the specimen. The temptation may be to ignore images with non-indexible patterns, but difficulties with indexing often clearly indicate that important structural information has been overlooked. Novices of image processing will benefit from studying the indexing examples presented in Misell's book (1978; pp.106-122) and cited in Table 1.I.D.8 of Baker (1981). Some aspects of the indexing of OD patterns are illustrated in Figs. III.69-72.

b. Filtering procedure

Once a set of diffraction spots is found to be consistent with a given lattice, a filter mask is designed with holes positioned to allow unobstructed passage of the diffraction spots at the lattice points (or lattice lines for helical particles). The mask is accurately positioned in the diffraction plane of the optical diffractometer so all spots at the lattice points are allowed through (Fig. III.73). Most of the aperiodic noise in the diffraction pattern, arising from non-periodic image features, is blocked out by opaque regions of the mask. A reconstruction lens, placed behind the mask, is used to refocus the unobstructed rays and forms a filtered image. If the mask is removed, an **unfiltered** image is formed. Optical reconstruction illustrates the Abbe double-diffraction phenomena of image formation (§ III.C.6.d): the diffraction pattern of the micrograph is formed in the first stage (forward transformation), and, in the second stage the reconstruction lens acts to rediffract the diffracted rays (back- or reverse transformation) to form an image (filtered or unfiltered). Thus, a filtered (or unfiltered) image is the result of rediffraction of the masked (or unmasked) diffraction pattern of the object (micrograph).

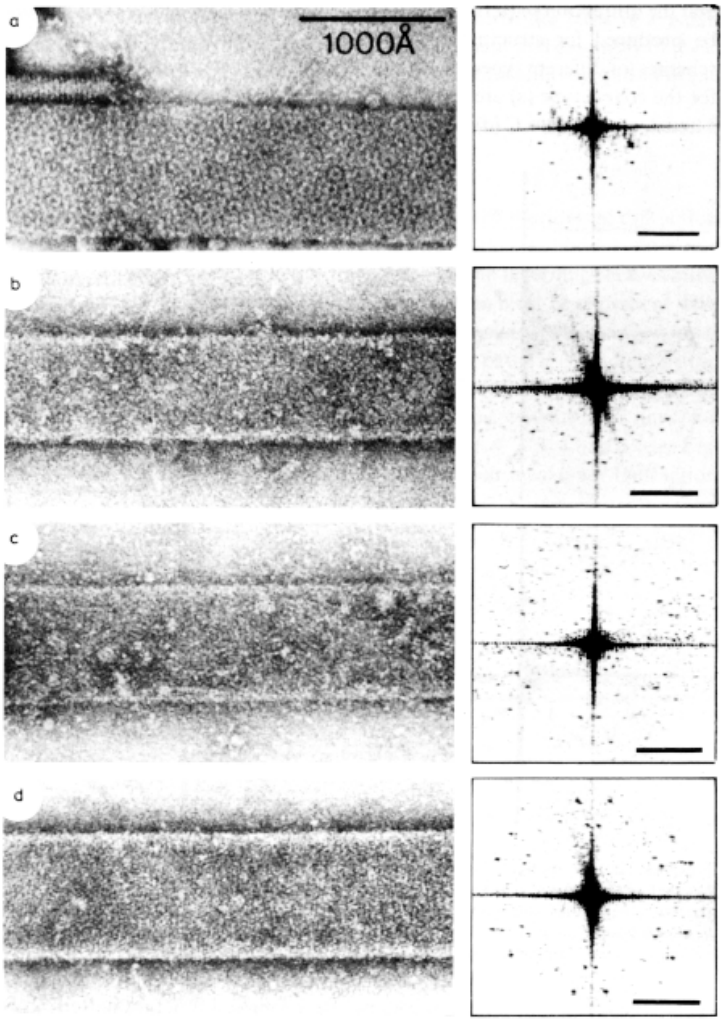

Fig. III.68. Electron micrographs and optical diffraction (OD) patterns of four different kinds of T-even bacteriophage polyheads. All specimens were negatively stained with 2% NaPT. (a) Coarse polyhead. (b) A-type polyhead. (c) B-type polyhead. (d) C-type polyhead. Differences in the OD patterns reflect differences (that can't be seen by naked eye) in the 'crystal' lattice structures. (From Steven *et al.*, 1976, p.192)

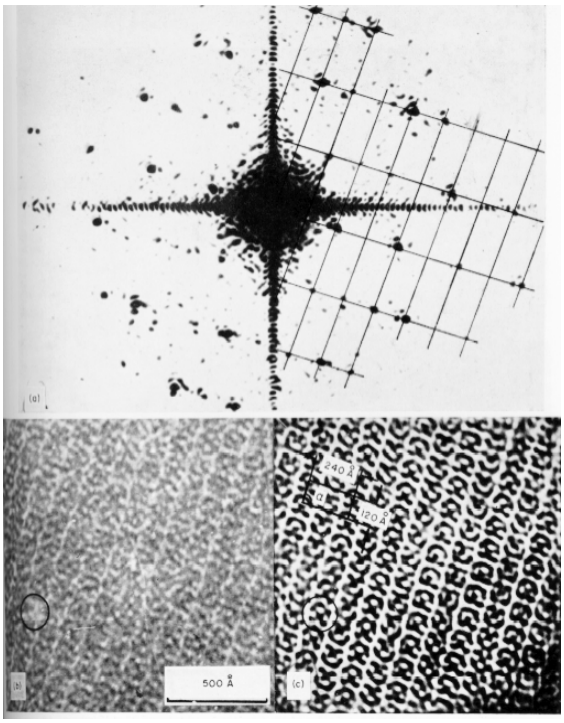

Fig. III.69. Optical diffraction of a portion of a plane layer of phosphorylase b particles and optical filtering of the image. (a) OD pattern (right hand part is indexed on the reciprocal lattice). (b) Portion of a 2D crystal before filtering experiment (stain here is white and protein is black). The particle in the circle is missing. (c) Filtered image. The missing particle shows up as a result of the averaging action of filtering. The unit cell shown on the image corresponds to the reciprocal lattice of (a). (From Kiselev *et al.*, 1971, Plate III)

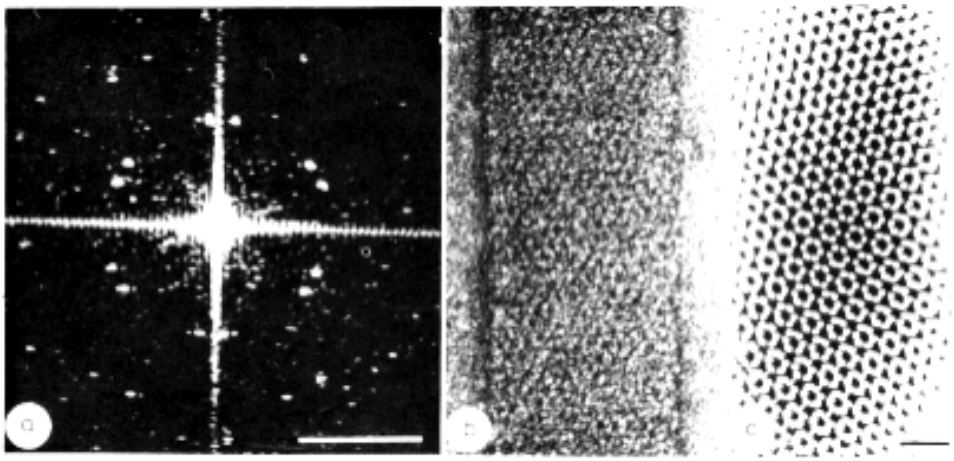

Fig. III.70. (a) Optical transform obtained from (b) micrograph of negatively stained bacteriophage T4 polyhead (coarse). (c) One-sided optical reconstruction of the polyhead lattice. Scale bar in filtered image = 20 nm. Scale bar in OD pattern = $0.2nm^{-1}$. (From Misell, 1978, p.116)

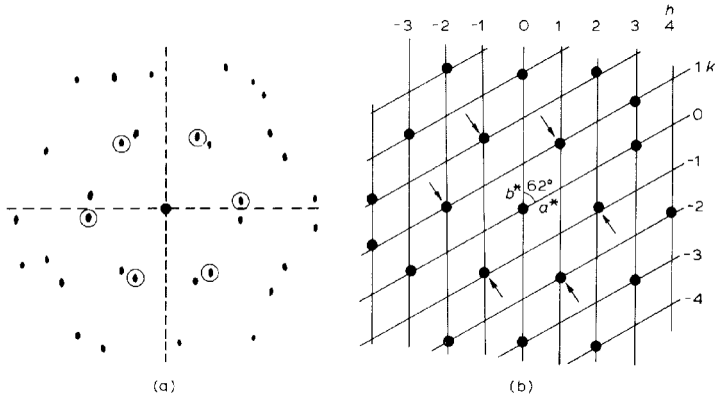

Fig. III.71. Reciprocal lattice for the coarse polyhead shown in Fig. III.70. The first order of the hexagonal lattice is missing. Note also that these schematic representations of the OD pattern (a) and one side of the reciprocal lattice (b) are rotated 90 degrees with respect to the OD pattern depicted in Fig. III.70. (a) Original OD pattern with spots from one-side ringed. (b) Reciprocal lattice drawn through the spots resulting from one-sided diffraction (arrowed). (*h,k*) define the diffraction order; *a** and *b** are the reciprocal lattice constants. *a** = *b** for a hexagonal lattice. (From Misell, 1978, p.116).

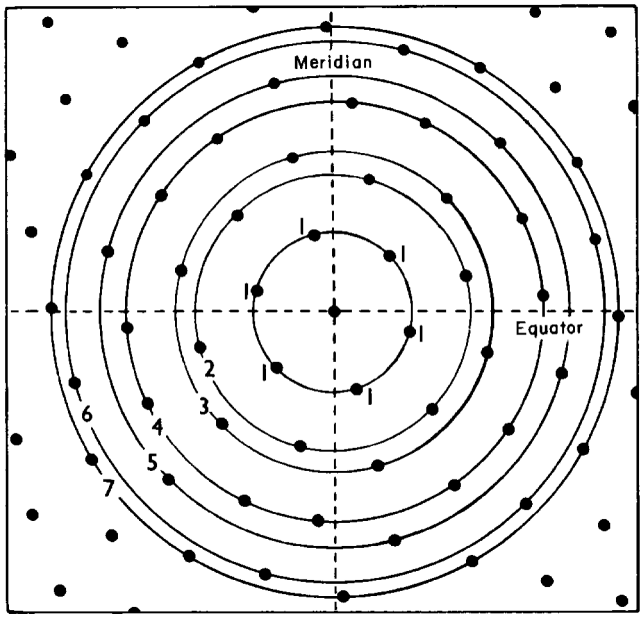

Fig. III.72. A capsomer with 6-fold symmetry convolved over a hexagonal lattice generates a diffraction pattern in which the Fourier transform of the capsomer is sampled on a hexagonal reciprocal lattice. The 6-fold symmetry of the capsomer is reflected in its Fourier transform in that, in the absence of noise, each diffraction spot is related to five other hexagonally conjugate spots. These sextets of equivalent spots lie on concentric circles that, in order of increasing radius, we refer to as 1st, 2nd, 3rd, etc. orders, as shown in the schematic drawing. The radii of these circles bear fixed ratios to one another (R_1:R_2:R_3:R_4 etc. = 1:$\sqrt{3}$:2:$\sqrt{7}$ etc.). In practice, sources of electron micrograph noise, as well as departures from exact symmetry, comprise the equivalence of hexagonally conjugate spots, but indexation of the diffraction pattern is possible provided at least two orders are visible. (From Steven *et al.*, 1976, p.194)

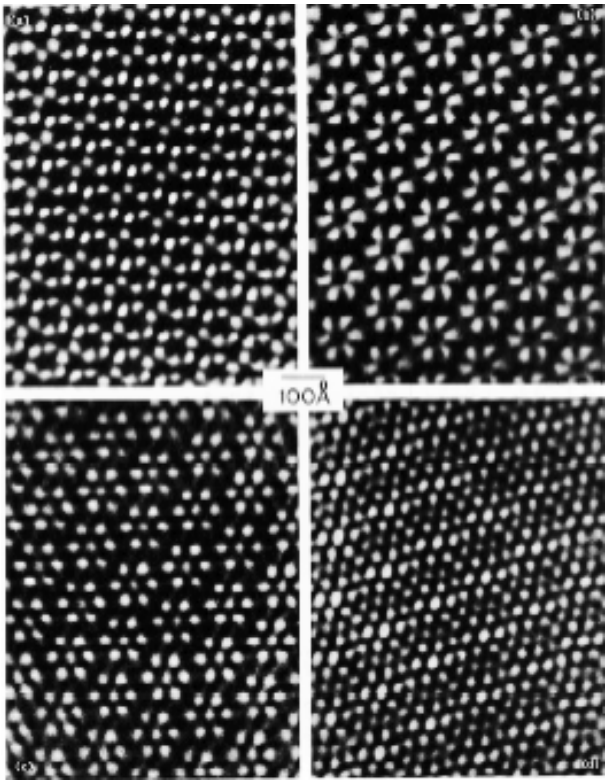

Fig. III.73. Optical filtrations of the four major classes of T4 polyhead as shown in Fig. III.68. Upper left: coarse polyhead. Upper right: A-type polyhead. Lower left: B-type polyhead. Lower right: C-type polyhead. (From Steven *et al.*, 1976, p.200)

c. Filtering apparatus (Figs. III.74-76)

Filtration experiments are performed on an optical diffractometer equipped with a reconstruction lens (or lenses). The reconstruction system must be of high optical quality to minimize image distortions (*e.g.* phase errors due to spherical aberration). Camera lenses often make suitable reconstruction lenses, although they are usually expensive and not ideally designed for the purposes of the optical reconstruction experiment (camera lenses are generally designed for optimum transmission of light, not for flatness of field). A high quality, but inexpensive, corrected doublet, with a large usable aperture, can produce quality, reconstruction images.

Usually a folded diffractometer (*e.g.* Fig. III.62) is employed both for survey and reconstruction work, mainly because it is more convenient to operate compared with a linear-type apparatus. The main disadvantage of the folded design is that mirrors are required to bend the optical light path. Mirrors add extra optical surfaces, which collect dust or become scratched and thus can deteriorate the quality of the diffraction pattern or reconstruction image. Expensive, high-quality (high reflectance and optically flat) mirrors are recommended for optimum results. The quality of the optical bench is easily assessed by critically comparing an unfiltered reconstruction with the original image. The closer the match, the better the reconstruction system.

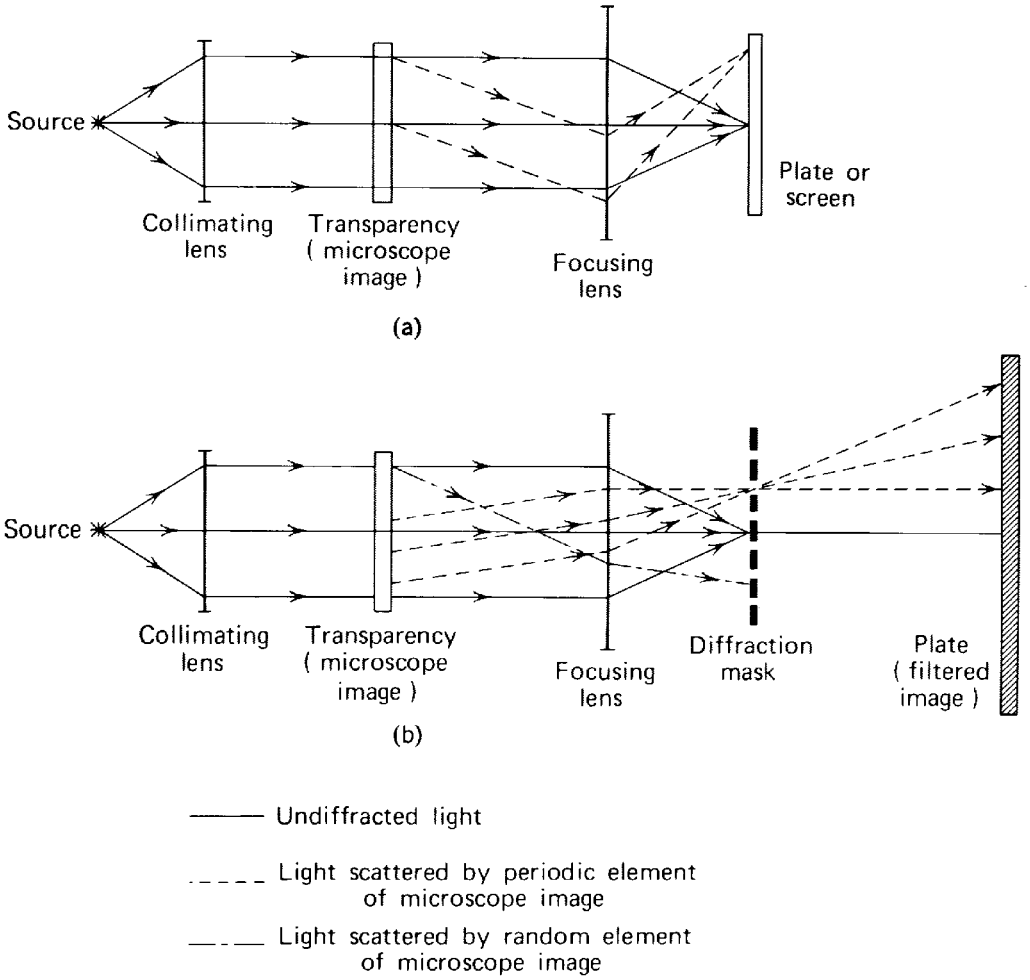

Fig. III.74. Optical filtering. (a) Recording of diffraction pattern. (b) Recording of the filtered image. Note that the paths of the dashed rays are inaccurate, because, for example, in (a) the ray that passes nearly through the center of the lens should bend only slightly (according to thin lens action, rays passing through the center of a thin lens will continue on a straight line. See § I.A.4). (From Slayter, 1970, p. 448)

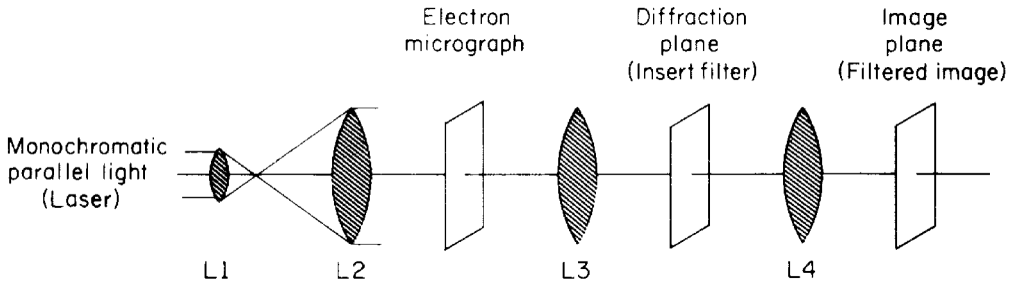

Fig. III.75. An optical system typically used to diffract and filter electron micrographs. (From Lake, 1972, p. 63)

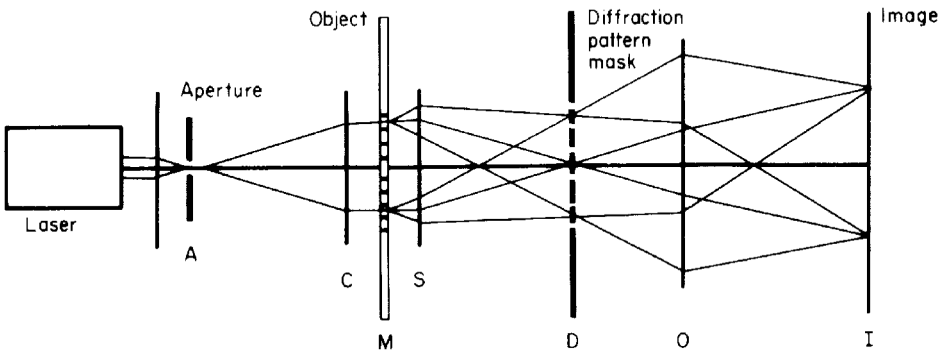

Fig. III.76. Schematic diagram of an optical diffractometer used to form a reconstructed image, I. C and S are the collimating and diffraction lenses, respectively, and O is the reconstruction lens. (From Blundell and Johnson, 1976, p.110)

d. Design of filter masks

Once a consistent indexing scheme is established, the design and fabrication of the filter mask (Table 1.II.E, Baker, 1981) usually constitute the rate limiting steps in a filtration experiment. Chemical etching procedures are used to produce precise masks: but, more tedious and demanding manufacturing skills are required compared to those for preparing masks by punching or drilling holes. Erickson, Voter and Leonard (1978) describe a simple method for producing suitable masks within minutes. Their method has the additional advantage of using the original, recorded pattern as a template.

e. Image averaging

Optical filtering reduces image noise by averaging neighboring, periodically repeated units in the array. As the size of holes in the filter mask is reduced, more noise in the diffraction pattern is removed and the extent of local averaging increases (Figs. III.77-79). That is, the image of a given unit in the array is averaged with more of its neighbors. If holes are made smaller than the diffraction spots, the signal-to-noise ratio may actually decrease (Table 1.II.F.1.d, Baker, 1981).

f. Artifacts of optical filtering

Filtered reconstructions often contain undetected, erroneous details as a result of several types of artifacts. Three obvious sources include 1) pattern mis-indexing resulting in incorrect mask design, 2) incorrect positioning of the mask in the diffraction plane causing spots to be partially or totally blocked, and 3) mis-positioned or mis-shaped mask holes making it impossible to pass all spots through the mask simultaneously. More subtle sources of artifact are indicated in Table 1.II.F of Baker (1981). Some authors contend that ALL reconstructions are, at least to some extent, erroneous (Berger *et al.*, 1972; Horne and Markham, 1972; Haydon and Scales, 1973; Taylor and Ranniko, 1974).

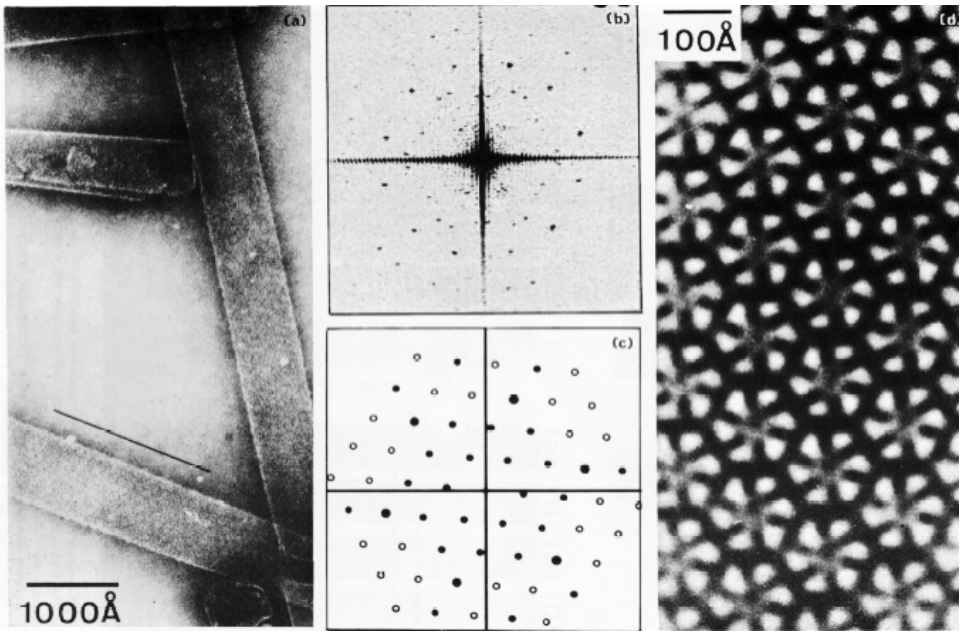

Fig. III.77. (a) Electron micrograph of AB-type T4 polyheads, negatively stained with 2% NaPT. (b) OD pattern of the marked region of the polyhead. (c) Indexation of the reciprocal lattice of the diffraction pattern generated by one side of the flattened polyhead bilayer. Visible diffraction spots are shown with solid circles, invisible ones with empty circles. For orientation, the dominant spots of the 4th radial order are shown with larger full circles. The other diffraction spots can be obtained from the Indexation by reflection of the given lattice through the meridian (vertical axis). (d) Optical filtration of this polyhead. (From Steven *et al.*, 1976, p.205)

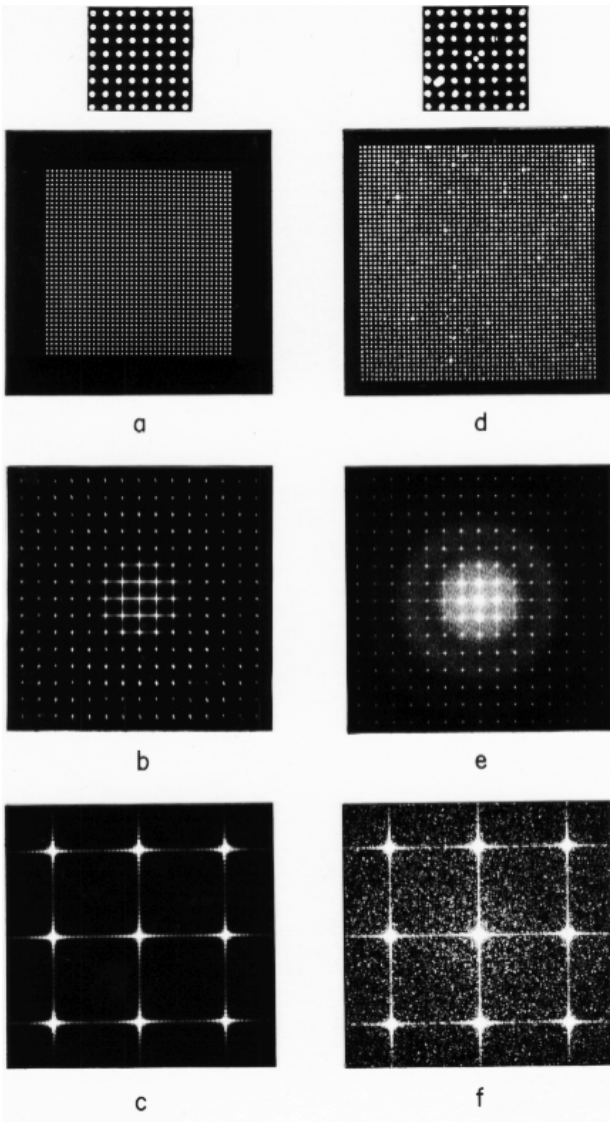

Fig. III.78. Optical filtering demonstration, Part 1. (a) 40 by 40 array of nearly 'perfect' circular holes, representing an idealized model of a crystal structure. A magnified portion appears directly above the complete array. The diffracting object is a copper foil with holes etched in it. (b) The OD pattern of (a). Note that the transform exists only at discrete lattice points (reciprocal lattice) except for the subsidiary maxima, which are shown more clearly in the enlarged view (c). Because (a) is the convolution of a circular hole with a 40 by 40 lattice of points, (b) is the transform of a single hole (Airy function) multiplied (or sampled) by a lattice, which is the reciprocal of the lattice of (a). (c) Enlarged central region of (b) showing the subsidiary maxima between lattice points. The subsidiary maxima contain information about the overall shape of the diffracting object. If n is the number of repeating units in a given direction, then the number of subsidiary maxima along the same direction in the transform is n-2. Thus, by counting the number (38 in this example) of maxima between two lattice points in (c), the number of repeating units (40) can be determined without seeing the object. (d) 50 by 50 array of imperfectly shaped holes representing a distorted crystal structure. The magnified region (above) also shows an extra hole, which does not belong to the rest of the lattice. (e) Optical transform of (d). A large portion of the diffracted light falls between the lattice points, indicating the presence of aperiodic information in the object (d). (f) Enlarged central region of (e).

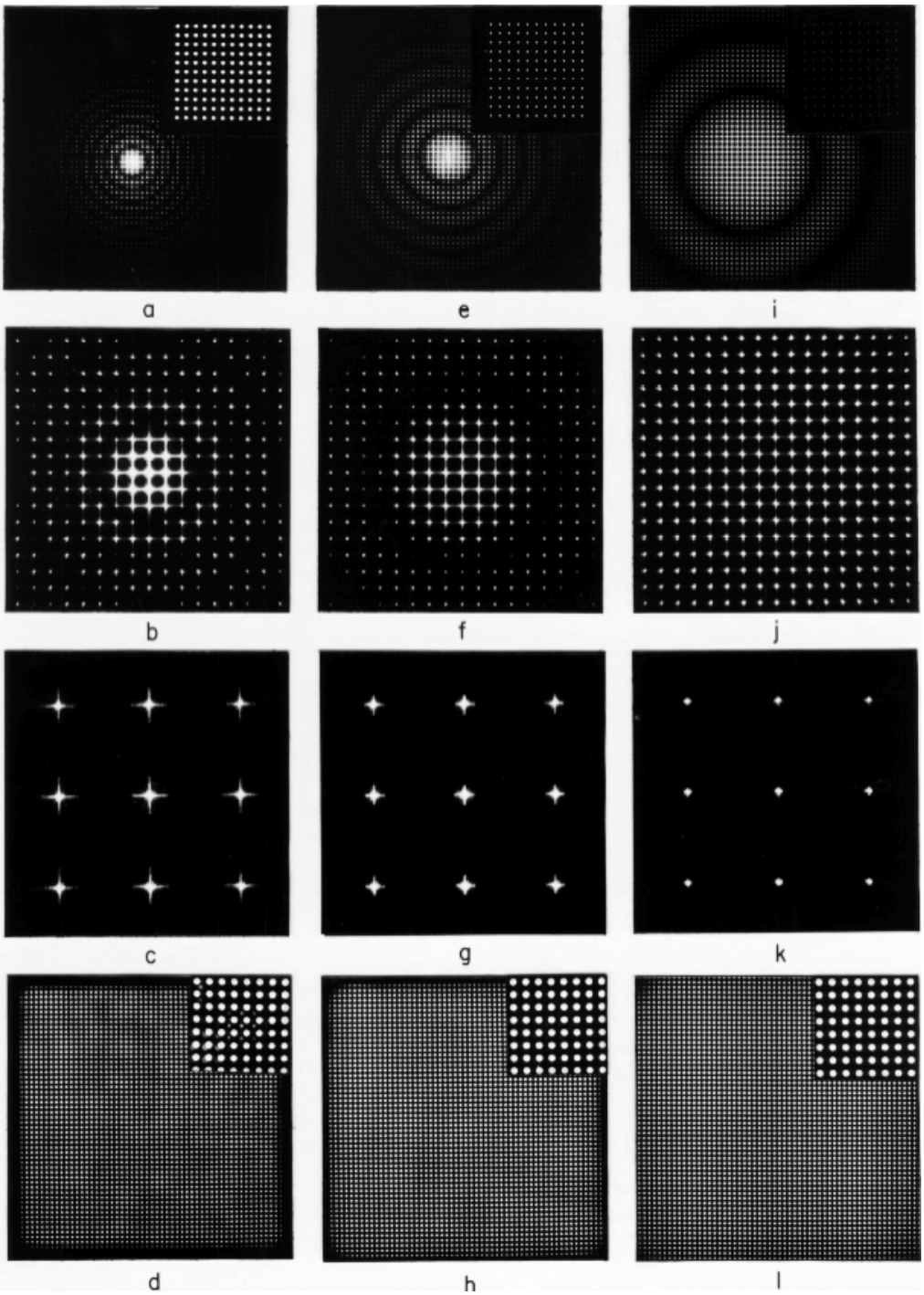

Fig. III.79. Optical filtering demonstration, Part 2. (a,e,i) Filtering masks (insets) and their transforms. The masks are identical 11 by 11 arrays except for the size of the holes. $d_{a^*}/a^* = 0.43$, 0.20, and 0.10 for the masks represented in (a), (e), and (i). The masks are designed to filter the central 11 by 11 array of the transform shown in Flg. III.78e. All three mask transforms have the same lattice parameters (which must be identical with the object lattice), but they are multiplied by the transform of the different size holes in each case. As the mask hole gets smaller, the area of the central maximum of the hole transform (Airy function) increases. The mask transform is the function that the object (Fig. III.78d) is convoluted with. Thus, the size of the central maximum is the area of local averaging in the filtered reconstructions (d,h,l). (b,f,j) Enlarged views of (a), (e), and (i), respectively. The number of lattice points contained in the central maximum is approximately the number of times each repeating unit of the object gets superimposed in the filtered reconstruction image. The numbers in these examples are approximately (b) 17, (f) 79, and (j) 314. (c,g,k) Same as Fig. III.78f with masks of (a), (e), and (i) positioned in the transform plane of the optical diffractometer. This shows what information is allowed to pass the transform plane of the diffractometer and recombine in the reconstruction plane. (Note: only the central 3 by 3 portion of the 11 by 11 array is shown here). (d,h,l) Filtered, reconstruction images of Fig. III.78d. The insets are from the identical region shown in the magnified portion of Fig. III.78d. Notice how the original 50 by 50 array of Fig. III.78d becomes larger in the filtered images.

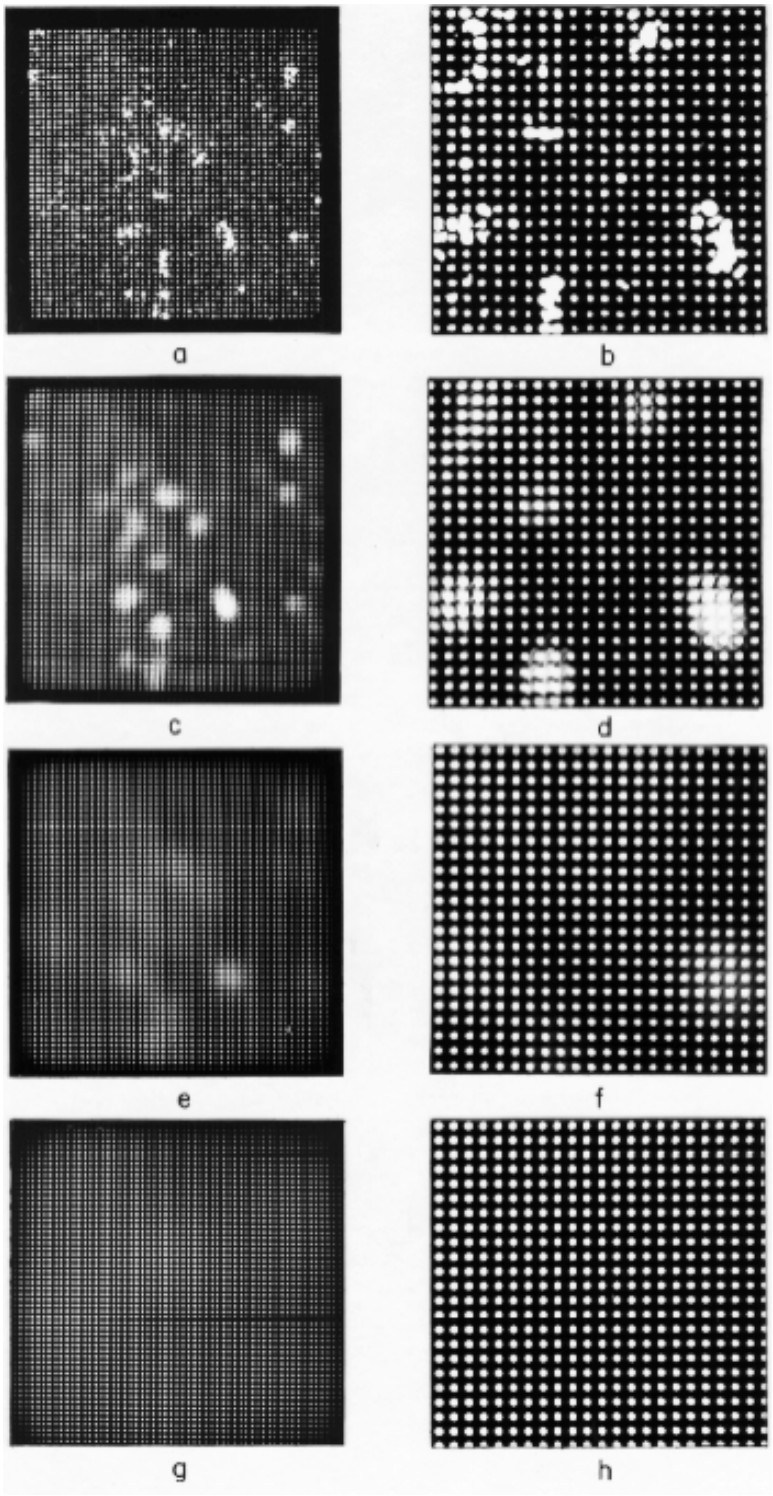

Fig. III.80. Optical filtering demonstration, Part 3: Very 'distorted' structure. (a) 50 by 50 array of an "imperfect" crystal with some very large defects. (b) Enlarged portion of (a). (c,e,g) Filtered images of (a) obtained using the masks of Fig. III.79 a,e,i respectively. (d,f,h) Enlarged views of (c), (e), and (g) from the same region as (b). Notice that the holes in the filter mask must be sufficiently small ($d_{a^*}/a^* = 0.1$) before the noise resulting from the major defects is averaged out. This also demonstrates how a periodicity can be forced on a structure by the action of the mask in Fourier space.

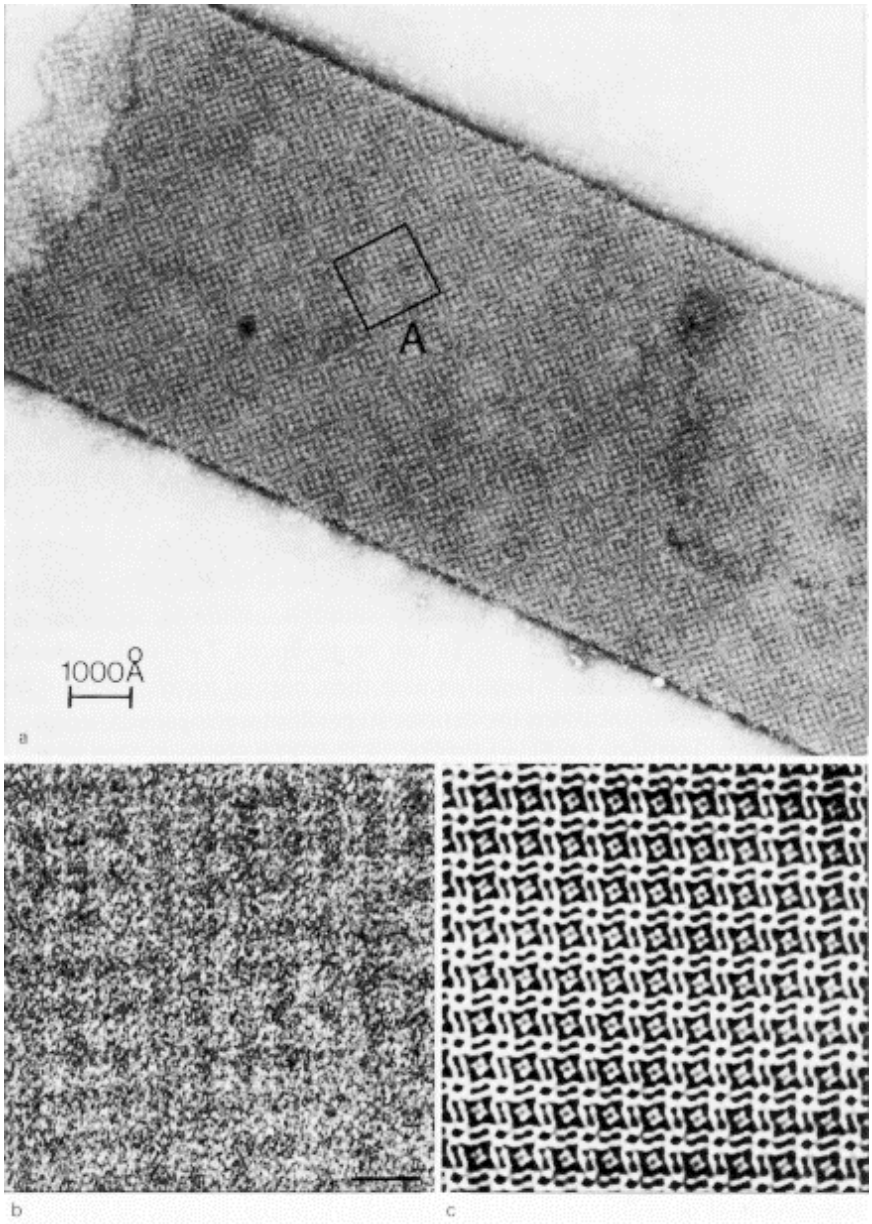

Fig. III.81. Optical filtering of double-layer crystal. (a) Image of negatively stained T-layer from *Bacillus brevis*. (b) Enlarged view of area A, consisting of about 10 x 10 unit cells. (c) Optical reconstruction of upper layer of area A. Bar in (b,c) = 200Å. (From Misell, 1978, p.163 adapted from Aebi *et al.,* 1973)

g. Comparison with translational photographic-superposition method

The **translational, photographic-superposition method** (also called linear integration: Markham *et al.*, 1964) produces analogous but **not** identical results with those of optical filtering (Figs. III.82-83). The translational parameters (lattice repeat and geometry) are best determined by optical diffraction, not by subjective, trial and error methods (Table 1.IV.B.1.a, Baker, 1981). Despite procedural differences, optical and digital filtering methods produce remarkably similar results (Aebi, *et al.*, 1973; Misell, 1978; Fig. III.84). Even though structural details may be reliably represented by either method, digital processing offers considerable advantages (discussed in § III.D.3).

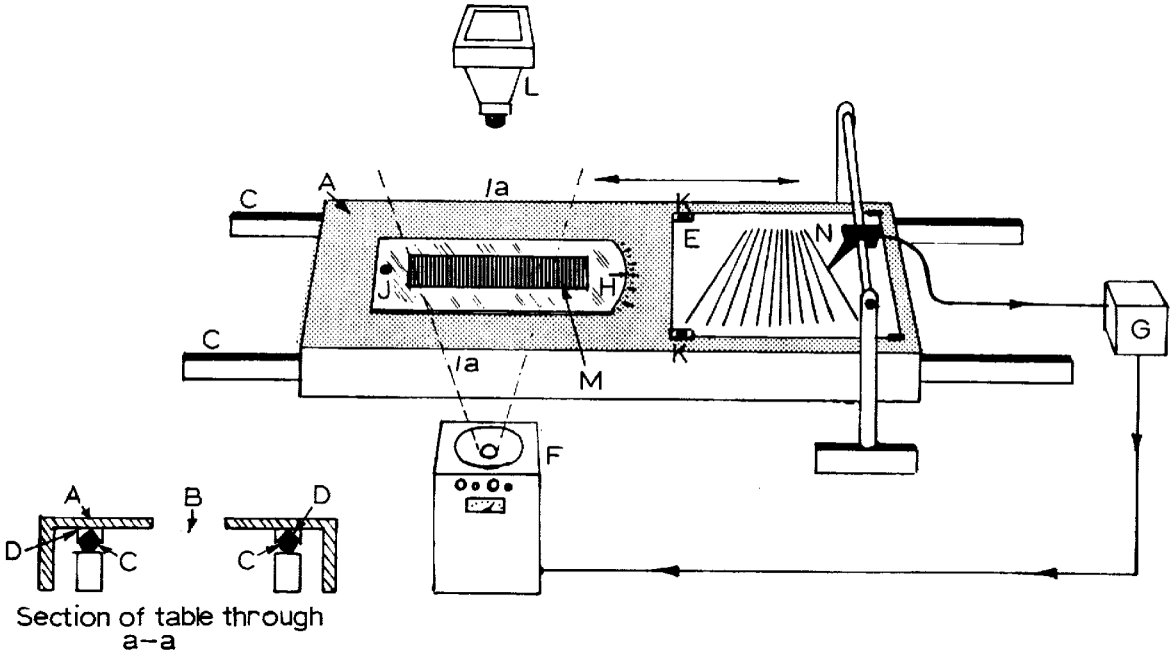

Fig. III.82. The basic arrangement of the linear integrator. (From Horne and Markham, 1972, p.421)

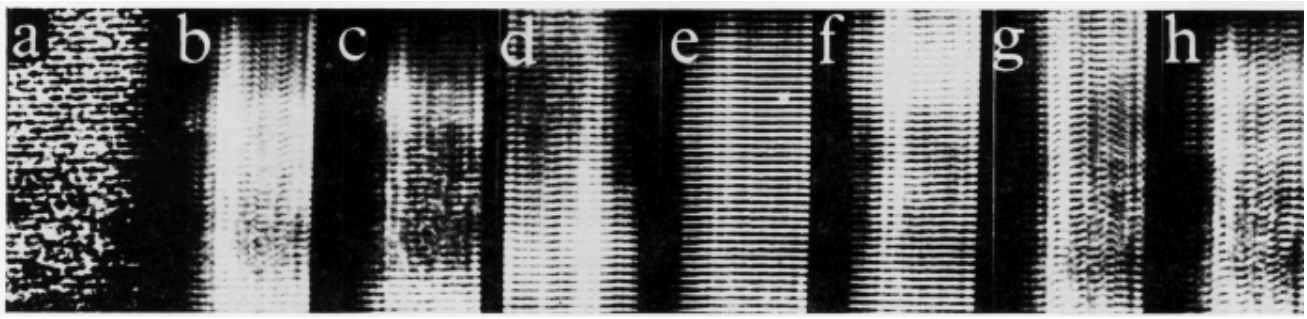

Fig. III.83. Electron micrographs showing repetitive features subjected to integration with the aid of the apparatus shown in Fig. III.82. The lattice spacings in Pt phthalocyanine crystals serve as a good illustration for the application of this technique to provide image reinforcement and accurate measurement. The series of photographs shows the original image (a) after integration at periodicities of b = 1.116, c = 1.142, d = 1.168, e = 1.194, f = 1.220, g = 1.246, and h = 1.272 nm respectively. (From Horne and Markham, 1972, p.422)

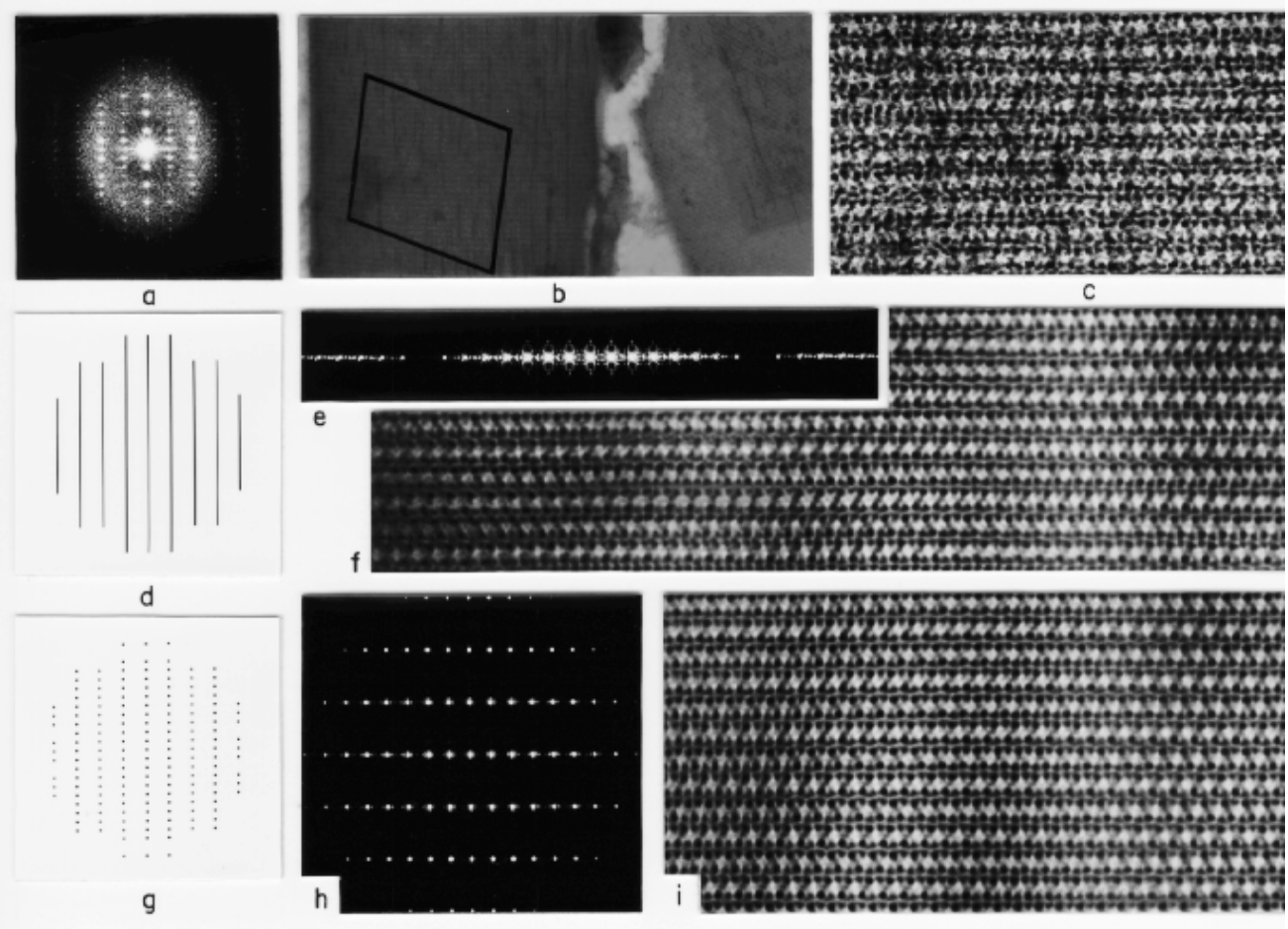

Fig. III.84. Optical filtering demonstration, Part 4. (a) Optical transform of a circular area of (b). (b) Low magnification image of a negatively stained catalase crystal. The parallelogram shaped area was processed in the filtering experiments (f) and (i). The shape of the window was chosen to minimize diffraction effects on the reconstruction images. (c) Enlarged portion of (b) from the region used for reconstruction. (d) Drawing of mask used for 1D filtering of (b). Magnification is same as in (a). (e) Central portion of the diffraction pattern of (d). (f) Filtered image of (c) obtained with the mask in (d). (g) Drawing of mask used for 2D filtering of (b). Magnification is the same as in (a) and (d). (h) Central portion of the diffraction pattern of (g). (i) Filtered image of (c) obtained with the mask in (g).

Image (f) is obtained by convoluting (c) with the 1D lattice in (e). The intensity of each lattice point in (e) and (b) is equal to the square of the superposition weight at that point. This is because the recorded diffraction pattern is the square of the object transform, since, in (e) and (h) the phase information is lost and only the intensity at each lattice point is recorded. (d)-(f) are an example of an optical analog of the Markham linear superposition method. Notice in (f) that the repeat units are averaged in the horizontal but not vertical direction. The extent of averaging is equal to the number of points (15) in the central maximum of the mask transform shown in (e). The number is actually smaller than this because at least half of the superpositions have weights too small to be noticed in the reconstruction (f).

The second filtered image (i) is obtained by convoluting (c) with (h). In (i), therefore, the repeat units are averaged with horizontal as well as vertical neighbors. (f) and (i) are similar except that (f) still contains vertical components of random or aperiodic noise.

h. Symbolic mathematical description of optical filtering

The concepts of convolution and sampling (§ III.C.6.g) provide a fundamental basis for understanding the principles of optical reconstruction. Image averaging is simply obtained by convoluting the unfiltered image (*i*) with the Fourier transform of the filter mask ($\mathcal{T}(M) = m$). Assuming ***M*** is correctly made and positioned in the diffraction plane of the optical diffractometer, then ***m*** will cause *i* to be convoluted with a lattice whose geometry exactly matches that of the crystalline lattice of the specimen imaged. In the following expressions, capital letters are used to designate functions in transform (reciprocal) space, whereas lower case letters denote object (real) space functions.

IMAGE SPACE	TRANSFORMATION SPACE	RECONSTRUCTION SPACE
image	*T(image)xMASK*	$image*T^{-1}(MASK)$
i	*IxM*	*i*m*

where $I \times M = I \times [L*H] \times W$

$i*m = i*[I \times h]*w$

$M = [LATTICE*HOLE] \times WINDOW$

$m = [lattice \times hole]*window$

DEFINITIONS:

x = multiplication operation.

* = convolution operation.

T = forward Fourier transform operation.

T^{-1} = inverse Fourier transform operation.

i = unfiltered, original micrograph (image).

I = *T(i*), the forward Fourier transform of *i*.

M = filter *MASK* (a physical entity in an optical filtering experiment).

m = $T^{-1}(M)$, the inverse Fourier transform of *MASK*.

L = *LATTICE* which "exactly" fits the reciprocal lattice of the crystalline object (*i*).

Recall that "*LATTICE*" is **infinite** in extent.

l = $T^{-1}(L)$, the inverse Fourier transform of *LATTICE*. This lattice "exactly" matches the real space crystal lattice **if *LATTICE* is chosen correctly.**

H = *HOLE* in the filtering *MASK* (usually circular ~20-50 μm diameter).

h = $T^{-1}(H)$, the inverse Fourier transform of *HOLE*. If *HOLE* is circular, *h* is an Airy function, that is, the Fourier transform of a *HOLE* which is mathematically defined as $J_1(X)/X$ (where $J_1(X)$ is a first order Bessel function).

W = *WINDOW* or boundary which limits the overall extent of the *MASK*.

w = $T^{-1}(W)$, the inverse Fourier transform of *WINDOW*. If the boundary of the *HOLES* in *MASK* is square or rectangular, *w* is a $\sin(X)/X$ function (a sharp "spike"). If *WINDOW* is circular, *w* is a $J_1(X)/X$, but note that *w* is a much sharper function than *h* because *W* is larger than *H* (Law of Reciprocity).

IxM = filtered diffraction pattern.

*i*m* = filtered image, or the original image convoluted with the Fourier transform of *MASK*.

III.D.3. Digital Fourier Analysis of Electron Micrographs

Processing images by digital rather than optical Fourier methods offers several advantages. The main advantages are that **digital methods are quantitative and adaptable.** In addition, procedures such as 3D reconstruction and rotational filtering are either impractical or essentially impossible to achieve with optical techniques. It is also not practical to carry out quantitative analysis and data manipulation on an optical bench. For example, image aberrations such as astigmatism and defocusing, or specimen distortions such as crystal lattice imperfections or curvature in filamentous specimens can be corrected more easily with digital procedures (Table 1.III.B.6, Baker, 1981). Diffraction amplitudes and phases can be measured and modified, for example, to correct for contrast transfer effects (see Table 1.III.C.3.g, Baker, 1981). Another advantage of digital processing is that separate image reconstructions can be averaged together and a measure of their agreement can be quantified (Table 1.III.B.3.b,c, Baker, 1981). Digital processing offers virtually infinite flexibility in data manipulation**.** For example, in "pseudo-optical filtering", the digital equivalent of optical filtering, filter masks with an infinite variety and combination of hole sizes, shapes, and "transparencies" can be designed with suitable software.

Computer image processing has replaced the requirement for high-quality, expensive optical systems. Nevertheless, there are **certain disadvantages** such as the necessity for discrete sampling of the data. This produces aliasing artifacts (transform overlap) that can be reduced, although never totally eliminated, by judicious choice of scanning conditions. DeRosier and Moore (1970) define and discuss the aliasing problem inherent to digital image processing.

The initial effort to set up a functioning digital system can be significant and one should be genuinely committed to image processing studies to warrant such effort. It is fruitless to develop a digital system just to view specimen diffraction patterns. An optical diffractometer is both inexpensive and operates at the speed of light! Optical diffraction is an excellent way to assess the quality of images since it is fast and inexpensive compared to digital methods, though digital methods continue to get faster and cheaper. Aebi, *et al.* (1973), Misell (1978) and the table below compare the advantages and disadvantages of optical and computer Fourier processing methods. Additional applications and selected examples of digital processing are outlined in Table 1.III.B of Baker (1981).

a. Comparison of optical and computer image analysis

Despite the obvious differences, optical and digital Fourier processing of electron micrographs are similar in many ways. The advantages and disadvantages of each of these procedures is summarized in the following table:

OPTICAL	COMPUTER
Original micrograph used	Micrograph digitized and "floated"
Bench required for diffraction can be simple and inexpensive	Requires fast computer to achieve “interactive” results
Formation of diffraction pattern instantaneous	Careful digitization is normally slow (> 10 min.) and computation of diffraction patterns may take several seconds or longer
Filtering operations require high quality (*i.e.* expensive) optics	Computers get more powerful and cheaper every day
Accurate filter masks tedious to make	Only limited by quality of software
Filtered image recorded photographically	Reconstructed images displayed and photographed using computer graphics devices
Quantitative information difficult or nearly impossible to obtain	Essence of computing IS to be quantitative
Amplitudes and phases difficult to manipulate	Infinite control over amplitudes and phases
Attenuation of zero-order beam to improve contrast in filtered image (may cause frequency doubling)	Control of contrast simple and straightforward

OPTICAL	COMPUTER
Imposing idealized, non-translational symmetries virtually impossible	Any symmetries (even incorrect ones!) can be easily imposed
Correction for lattice distortion virtually impossible	Lattice distortions can be corrected (*e.g.* reinterpolate original image onto perfect lattice)
Data (diffraction patterns and filtered images) are continuous (*i.e.* vary smoothly)	Data are discrete (pixels)
Fast for screening and selecting best images for additional analysis	Not yet, at least until CCD technology gets real cheap
Reconstruction of 3D structure essentially impossible	Procedures rather straightforward with "right" software
Impractical to average data from different micrographs	Easy to average data from different micrographs

b. Digital processing steps

A typical digital processing procedure includes the following steps:

- Image selection
- Densitometry
- Boxing and floating
- Fourier transformation
- Indexing 2D lattices (for objects with translational symmetry)
- 2D filtering/ 3D reconstruction

Image selection

After an initial screening by eye (to discard obviously bad images), micrographs are examined by optical diffraction to select a subset of the "best" images in terms of both optical quality and specimen preservation. This selected subset of images is then examined by digital processing methods. An optical diffraction pattern quickly reveals the electron optical conditions present when the micrograph was recorded (defocus level, astigmatism, drift, vibration, etc.). Note that optical diffraction is generally an unsuitable method for selecting images of individual particles with well-preserved symmetry, which might for example be suitable for digital, rotational filtering procedures (§ III.D.4.b). For this type specimen, the rotational power spectrum is computed from the digitized image and analyzed (§ III.D.4.b).

Densitometry

If the micrograph was captured on a CCD camera, no further digitization of the image is necessary and it is available for immediate boxing and floating as described in the next section. Micrographs recorded on film are digitized on a **scanning densitometer**, a device that converts optical densities on the photographic emulsion to a digital image (a numerical array corresponding to the optical densities at discrete positions in the image). Several types of densitometers are available for digitizing TEM images. The most precise (hence, most expensive) are the flatbed type devices (*e.g.* Figs. III.85-86), which are used to digitize the micrograph while it lays flat. In older, rotating-drum densitometers, the micrograph is fixed to a cylindrical surface (drum) and the micrograph is scanned while it is translated along and rotated about the drum axis.

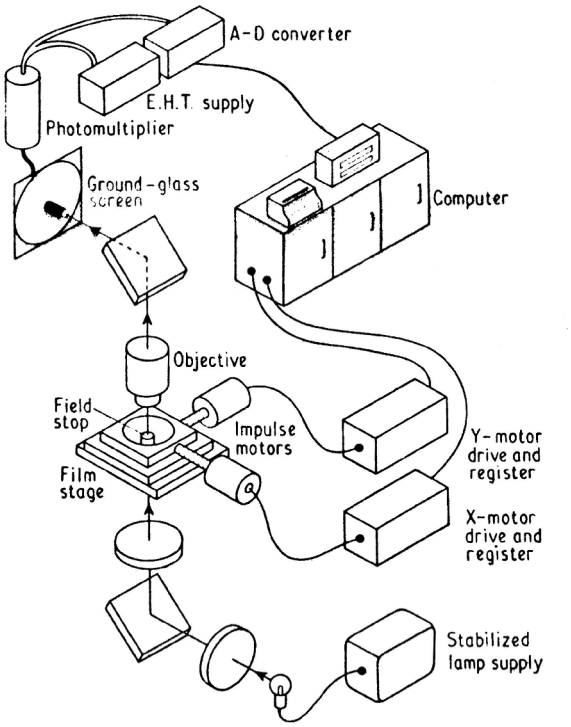

Fig. III.85. Schematic view of the principal parts of a flatbed microdensitometer. (From Arndt *et al.*, 1969, p.386)

Fig. III.86. The Zeiss Photoscan densitometer is generally used to scan images at a pixel step size of 7 μm. (From Scripps Research Institute CIMBio web site)

The density value at each point in the digitized image is represented as a **pixel** with intensity ranging between 0 and 255 (an eight-bit number) or 4096 (12-bit number) or even higher in some CCD cameras. The information contained in a single 1024 by 1024 digital image (1,048,576 pixels), which is quite small by today's standards, is quite staggering: it is roughly equivalent to slightly more than the **entire** contents of the lecture notes (text only) for this course. Note that, at a raster step size of 7 μm (smallest step size on the Zeiss flat-bed densitometer shown in Fig. III.86), the area of the micrograph digitized for a 1024 by 1024 array would be ~50 mm^2 or only 0.625% (1/160th) of the entire area of a typical 8 x 10 cm micrograph. The amount of 'information' contained in a single TEM micrograph is impressive if not mind-boggling.

Images are scanned at raster settings corresponding to dimensions that are **one-third or less** of the expected resolution in the image to minimize aliasing artifacts (Table 1.III.C.2.c, Baker, 1981; Figs. III.87-88). The equivalent step size or pixel resolution in the specimen image depends on the magnification of the micrograph that is scanned. For example, if the micrograph was recorded at a magnification of 45,000X and scanned at 14 μm intervals, then each pixel corresponds to 0.311 nm at the specimen. The **maximum resolution** one could reasonably expect to recover from such a digitized image is thus about 0.933 nm (= 3 x 0.311). This of course assumes the specimen is preserved to *at least* this resolution **and** the electron optical conditions allow recovery of this level of detail. The table below lists the pixel size at the specimen (in nm) for images at recorded at different nominal magnifications and scanned at four different step sizes such as those available, for example, on the Zeiss microdensitometer (Fig. III.86). Using the above rule of thumb, the maximum

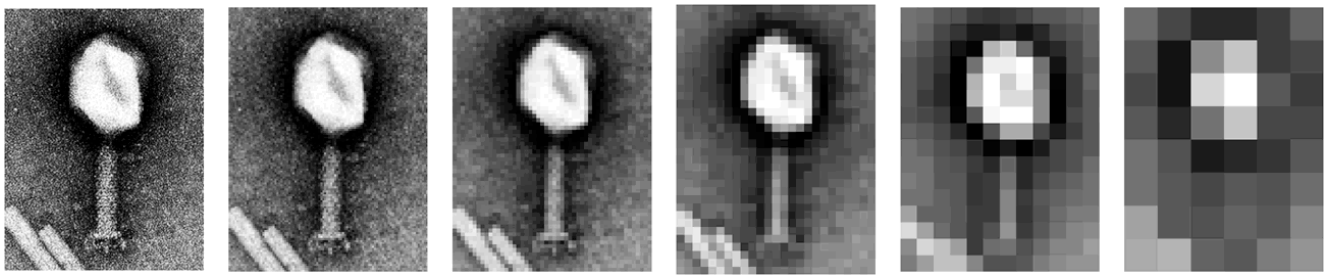

Fig. III.87. Scanned image of negatively stained bacteriophage T4, sampled at different step-sizes. Left to Right: 200, 100, 50, 25, 12, and 6 dpi (dots per inch).

resolution recoverable for any size pixel will be about three times larger than the corresponding pixel size.

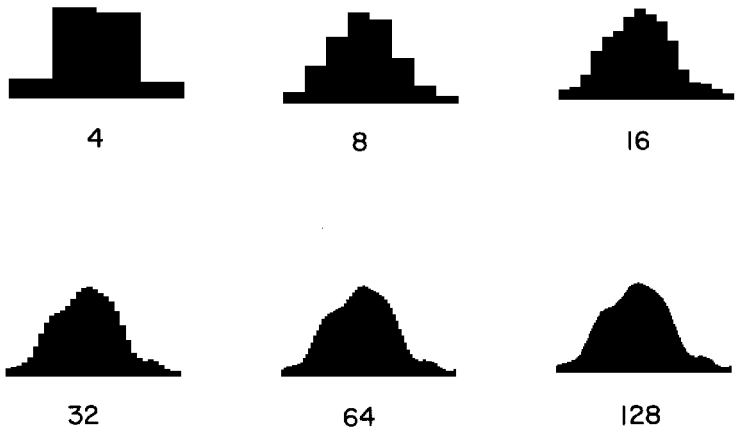

Fig. III.88. Effect of sampling interval on recovery of information. In this example, an arbitrary function has been sampled at 4, 8, 16, 32, 64, or 128 intervals. A sampling interval of 32 appears to be just fine enough to recover the shape of the 1D function without loss of information. At coarser sampling intervals (4-16), the subtler features in the data are lost. In practice, one aims to digitize the data at a fine enough interval to be certain that no information is lost. Thus, using the three-times pixel resolution criteria, in this example one ought to sample the data 96 (= 3 x 32) or more times to be certain to recover all the information contained in the data.

Pixel Size at Specimen (nm)

FEI CM300 MICROGRAPH MAGNIFICATION	ZEISS PHODIS SCAN STEP SIZE (μm)			
	7	14	28	56
13,500	0.519	1.037	2.074	4.148
19,500	0.359	0.718	1.436	2.872
24,000	0.292	0.583	1.167	2.333
33,000	0.212	0.424	0.848	1.697
45,000	0.156	0.311	0.622	1.244
61,000	0.115	0.230	0.459	0.918

Microdensitometers are computer-controlled devices. They measure optical densities in the micrograph on a square grid (*i.e.* at equal-spaced intervals in *x* and *y* directions: Fig. III.85). The change in intensity of a small beam of light after it passes through the micrograph is measured using a photomultiplier, which converts the analog signal (beam of light) to a digital signal (intensity value typically between 0 and 255). The digitized data can be displayed directly on a computer graphics screen or stored on various media (*e.g.* disk drive or CD or DVD) for archival purposes and subsequent manipulations. As mentioned above, digitized images often contain significantly large amounts of data (pixels), and they can quickly fill up the storage capacity of disk drives on computers. Several years ago, before the days of high capacity storage technology, large (2400'), 1600 bpi (bits per inch), 9-track magnetic tapes were used for data storage and each tape only held about 25 1024 by 1024 images (each pixel stored as a 16 bit value). Today's students are too young to remember the double-sided, single-density floppy diskette once used in personal computers that could only store 360 Kbytes (here one byte = 16 bits), which was barely sufficient to store ***one*** measly 512 by 512 image. If an entire micrograph is scanned at a 7 μm step size, there will be roughly 10,000 by 14,000 pixels. If each pixel is represented as a 4-byte, floating point number, the scanned micrograph will consume more than one-half Gigabyte (Gb) of storage capacity (10,000 x 14,000 x 4 = 560 Megabytes). Hence, only one entire micrograph scanned in this manner could fit onto a single 650 MB CD. More and more image reconstruction labs now use database storage technology to help manage the bookkeeping, retrieval, and processing of these large amounts of digitized image data.

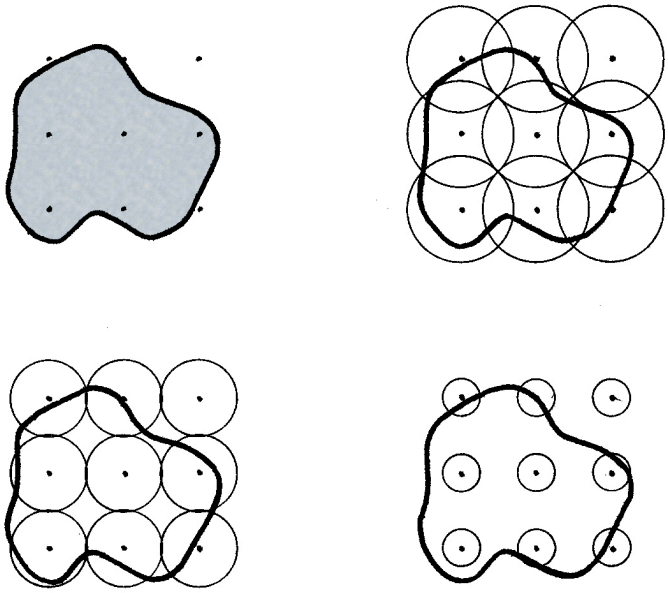

Fig. III.89. Diagrammatic representation of sampling a 2D image on a square lattice. Upper left shows the sampling if it could be performed at discrete points. Lower left shows the usual situation in which the diameter of the illuminating light beam exactly matches the sampling interval. In the upper right panel, the illuminating beam is larger than the raster step, which leads to smearing of information because the intensity of the image in neighboring regions gets averaged in with the intensity of the area adjacent to each lattice point. The illuminating beam in the lower right panel is too small, thus only a small fraction of the area defined by the sampling lattice is illuminated about each point. The ideal situation would occur if the image could be illuminated with a square beam, whose dimensions exactly matched the sampling lattice. This is not accomplished in practice.

Boxing and floating the digital image

The entire digital image or selected (**boxed or windowed**) areas may be used for subsequent processing steps. If only a portion of the scanned image is needed, the area of interest is boxed in a manner similar to that used to mask micrographs for optical diffraction and filtering experiments. Thus, areas outside the biological specimen (*e.g.* carbon film or neighboring specimens, etc.) can be selectively removed since these areas mainly contribute noise to the image. Boxing is conveniently performed directly with the digital image displayed on a computer graphics monitor.

Regions of the digital image outside the area of interest are zeroed (equivalent to masking out an area of the micrograph for optical diffraction) and the numerical image is "**floated**" by subtracting the average image intensity around the perimeter of the boxed area from ALL image intensities within the masked area. Floating suppresses intense diffraction spots generated by edges of the masked area. The characteristic "cross" observed in optical diffraction patterns is caused by the strong diffraction that occurs at the edges of the square or rectangular mask where the contrast is much higher compared to that within the windowed portion of the micrograph. As you encounter pictures of diffraction patterns in the literature, make note of the presence or absence of the strong diffraction peaks near the center of the pattern. The presence of a strong spike or other diffraction at the center of the transform indicates that the pattern was most likely generated optically. Alternatively, if the pattern was generated on a computer and still shows strong diffraction spikes or other such effects, this would signify that the image was not floated properly before Fourier transformation.

Fourier transformation

Fourier transformation of the numerical array is usually computed by means of Fast-Fourier methods (Table 1.III.C.3.c, Baker, 1981). In many software packages, the boxed image is 'padded' to produce a larger image with pixel dimensions equal to some power of two (*e.g.* 64^2, 128^2, 256^2, 64x512, etc.). Thus, if the original boxed image was a 55 by 450 pixel array, then this image would be padded AT LEAST out to a 64 by 512 array and then Fourier transformed. Padding just adds pixels with zero intensity to the columns and rows of the boxed image array to make it meet the power of two criteria. This is NOT an essential criteria but it can lead to faster computation of the Fourier transform because some fast-Fourier transform (FFT) computer algorithms are more efficient with images sized this way.

The Fourier transform of an *n* by *m* image results in an *n* by *m* array of complex numbers. Each complex number represents one structure factor (§ III.C.6.f). Each structure factor is stored in computer memory either as a structure factor amplitude and phase or as the real (A-part) and imaginary (B-part) parts of the Structure Factor (§ III.C.6.f). Diffraction amplitudes and phases may

be displayed in a variety of ways, but typically on a computer graphics screen.

Indexing of two-dimensional lattices

As has already been emphasized, successful application of image analysis and processing procedures requires correct indexing of diffraction patterns. For well-ordered, 2D crystalline biological specimens, the diffraction pattern is dominated by a series of discrete spots (Bragg reflections) that lie on a reciprocal lattice. Such patterns are usually fairly easy to index (*i.e.* define the reciprocal lattice parameters and assign Miller indices to each of the spots). Recall that indexing is often already accomplished as a consequence of having inspected an optical diffraction pattern of the specimen image. The indexing of multilayered or two-sided structures (*e.g.* biological aggregates with helical symmetry) can be quite tricky, so care must be used before proceeding to the next step (filtration and reconstruction).

2D Filtering / 3D Reconstruction (Back-transformation)

Correct indexing of a diffraction pattern is tantamount to deciding which regions of the Fourier transform are attributed to 'noise' and which regions are attributed to 'signal'. Once the decision is made as to what is signal and what is noise, the computed Fourier transform is 'masked' in a manner completely analogous to the process used to mask the diffraction pattern on an optical bench (§ III.D.2). Thus, the amplitudes in the computed Fourier transform are zeroed everywhere except at the reciprocal lattice points. In **pseudo-optical filtering**, the term "points" actually refers to the transform values within a finite region ('holes' in the filter mask) centered at the mathematical points of an ideal reciprocal lattice: each transform value is left unmodified or may be weighted according to its distance from the ideal lattice (a point lying at or very near the ideal lattice would by multiplied by 1.0 whereas one near the edge of a mask 'hole' would be multiplied by a number close to zero). The modified ("filtered") diffraction pattern is subsequently mathematically back-transformed to reconstruct an averaged image. **Complete Fourier averaging** (all unit cells are averaged together with equal weight) is accomplished by reducing the entire transform to a single structure factor amplitude and phase at each of the reciprocal lattice points and reconstructing the structure of a single unit cell by Fourier synthesis (§ III.C.6.c).

There are numerous ways to render and display reconstructed image data. 'Old-timers' (and readers of the pioneering image processing literature) will recall the use of character over-printing on line printers, contour plotting, cathode ray density plotting, film writing, etc. (see Table 1.IV.B of Baker, 1981 for citations of examples). Modern computer graphics devices provide a variety of ways to render 2D or 3D reconstructed data in clear, interpretable form.

If the 3D structure of a particle is to be reconstructed, structure factor phases and amplitudes must be determined in three dimensions to fill in and generate a complete, 3D Fourier transform (see Fig. III.59). This is accomplished for a 2D crystal structure by combining structure factor data from several 2D diffraction patterns of independent views of the crystalline specimen. The extent of the 3D transform, and hence ultimate resolution that can be computed, depends both on the number and uniqueness of the specimen images that are included in the data set. Note that, in theory, one could add an 'infinite' number of images to achieve 'infinitely' high resolution, but, in reality, the actual resolution is limited by many other factors (*e.g.* radiation damage to the specimen, specimen distortions, image drift and astigmatism, defocus level, etc.).

The rationale for collecting and combining information from distinct views differs depending on the nature of specimen (*e.g.* is it helical, spherical, 2D, 3D, etc.) being studied (§ III.E).

c. Hardware/Software

Two obstacles of digital processing are the expense and complexity of the required hardware (microdensitometer and computer) and software (programs for carrying out the image processing procedures). Most structural biology (particularly protein crystallography) laboratories are equipped with the needed hardware, and often have programs (for example, Fast-Fourier transform, film scanning, and computer graphics routines) that can be adapted for most, basic image processing tasks. Microdensitometers can cost well over $100,000 for precision, flatbed

instruments (*e.g.* Fig. III.86). Most multi-user image processing can be performed quite adequately now on computer graphics workstations and even PCs costing a few thousand dollars.

Several of the laboratories deeply engaged in digital processing studies prefer to tailor their own computer software systems since the programs can then be designed to efficiently analyze specimens of particular interest to that lab. In this way, the learning curve is less steep for new lab members and results become easier to understand and interpret. If a highly specialized system is not essential, the use of various multipurpose software packages developed by others can be downloaded and used. Three of the more popular program packages currently available include SPIDER (Baxter *et al.,* 2007), IMAGIC (van Heel *et al.,* 1996), and EMAN2 (Tang *et al.,* 2007). Use of these packages can save considerable effort not to mention the frustrations of developing and testing *de novo* programs. The main disadvantage of "black-box" systems is the danger of incorrect implementation by untrained or inexperienced users.

III.D.4. 2D Digital Fourier Reconstruction Methods

Images of biological specimens can be processed in a variety of different ways, some of which are more popular or better established than others. Most processing methods are relatively straightforward, but occasionally one will encounter a difficult specimen that may require the use of a novel strategy. In general, the type of specimen examined dictates the type of method applied. A convenient classification of specimens can be made according to the shape or symmetry of the specimen.

Though ultimately our interest is in learning the full three-dimensional structure of the molecules that we image in the microscope, it can be quite informative to compute image reconstructions by Fourier methods in two dimensions, or sometimes even in one dimension (*e.g.* helices). Also, a large number of biological macromolecules such as membranes, cell walls, and some naturally occurring crystals are planar (2D) objects and make excellent subjects for Fourier image processing in 2D or 3D.

a. 2D Fourier averaging of specimens with 2D translational symmetry

Planar objects are considered 2D because one dimension is smaller or much smaller than the other two. For many specimens that fit this description, the shortest dimension is often 50 nm or smaller and includes only one or a few unit cells in the direction normal to the plane of the specimen (parallel to the electron beam when the specimen is untilted in the electron microscope). Though these type specimens can be analyzed with optical or photographic superposition methods, the digital Fourier methods are particularly powerful because they are quantitative and rigorous.

The methods and applications of 2D Fourier image processing for analyzing images of planar specimens can be found in numerous primary literature articles (see Reference Reading List, pp.28-30, for several examples). Examples of planar specimens that have been studied by 2D and 3D reconstruction techniques are the purple membrane, cytochrome oxidase vesicles, membrane-bound ribosomes, actin filament bundles and actin sheets, tubulin sheets, bacterial cell layers, RNA polymerase crystals, gap junction membranes, and tropomyosin crystals to name a few.

The following list briefly outlines the basic steps involved in analyzing in 2D the images of regular (*i.e.* highly ordered or crystalline) planar specimens. After the basic strategy is outlined, several figures are included to help illustrate various aspects of the procedures (Figs. III.90-III.96).

Protocol for Fourier averaging images of 2D crystals:

1) After a visual screening step (to toss obvious bad micrographs), select a subset of micrographs that give the highest quality optical diffraction patterns. Highly coherent crystalline areas give strong, sharp Bragg reflections to 'high' resolution (*e.g.* ~15-20Å for negatively stained crystals recorded with minimum irradiation techniques or even higher for unstained, frozen-hydrated specimens). Look for minimal radiation damage, astigmatism, and specimen drift or vibration and for 'best' defocus (*i.e.* giving the desired CTF characteristics) and highest resolution (most spots in all directions).

2) Digitize the micrograph at a sampling interval fine enough *not* to limit image resolution but not too fine or the digitized image will consist of many more pixels than is necessary, which results in needless computations.

3) Box (window) out the desired region of interest, making sure to exclude, if possible, as much of the unneeded portions of the digitized image as is practical. This is easy to do with 'perfect' specimens like catalase crystals that grow large enough (several μm^2) to fill the entire field of view at 30,000 magnification or higher.

4) Float the boxed image by subtracting from every pixel within the image the average value of the pixels that form the **perimeter** of the box.

5) Fourier transform the boxed, digitized image. With some software, the image must first be padded with zeroes so the image that is transformed has dimensions that are a power of two such as 256^2 or 512^2 or 256 x 512 or 128 x 1024, etc. Generally, owing to Friedel's Law, just the 'top half' of the Fourier transform need be computed (*i.e. k* values 0 or positive only). The transform is stored as structure factor A (real) and B (imaginary) parts. Hence, for a 512^2 image, the resulting transform will consist of 512 by 256 complex numbers.

6) Display and index the diffraction pattern on a graphics workstation. This indexing could be performed on an optical diffraction pattern, however, the digital transform allows one to quantitatively check other properties of the specimen such as the presence of certain plane group symmetries. The existence, for example, of a three-fold axis of symmetry at the unit cell origin, for noise free data, will restrict the structure factor phases to be multiples of 120°. The noisier the image the more the symmetry related structure factor phases will deviate from the 120° relationship.

7) Perform either pseudo-optical filtering or Fourier averaging of the data. In pseudo-optical filtering, filter masks can be computer generated with 'holes' of a specified size distributed on a lattice either covering the whole transform or limited at some specified upper resolution boundary. The computer-generated mask is then multiplied times the Fourier transform and the result is back-transformed to generate the filtered image. A number of variations of pseudo-optical filtering can be employed. For example, low and/or high-pass as well as lattice filter masks can be generated to perform different types of filtering of the data. Also, the holes can be given a Gaussian weight so the value at the center of the hole is 1.0 but then drops to 1/exp at the edge of the hole where the mask has a value of zero. The Fourier filtered image is obtained by back transforming the masked transform.

   To compute a Fourier-averaged reconstruction, in which **all** unit cells within the boxed area are averaged together, the data in the vicinity of each Bragg reflection are averaged or integrated together or are sampled to reduce the data to a single structure factor. This is equivalent to the pseudo-filtering experiment in which the hole size is reduced to zero radius, which has the effect of convoluting the image with a lattice that includes every unit cell contained within the boxed region of the micrograph. This convolution forces the image to obey a perfect translational symmetry (*i.e.* p1 plane group). Again, a number of variations of this process can be implemented to produce different Fourier averages. The average structure of a single unit cell (all unit cells are identical in a Fourier average) is obtained by back transforming the structure factors (Fourier synthesis).

8. Assess and apply additional symmetry if evidence exists that the specimen obeys symmetry higher than p1. This must be performed with due caution because it is very easy to apply ***any*** symmetry you want with computer programs. Hence, when you impose additional symmetry, the specimen will, of course, exhibit whatever symmetry has been applied.

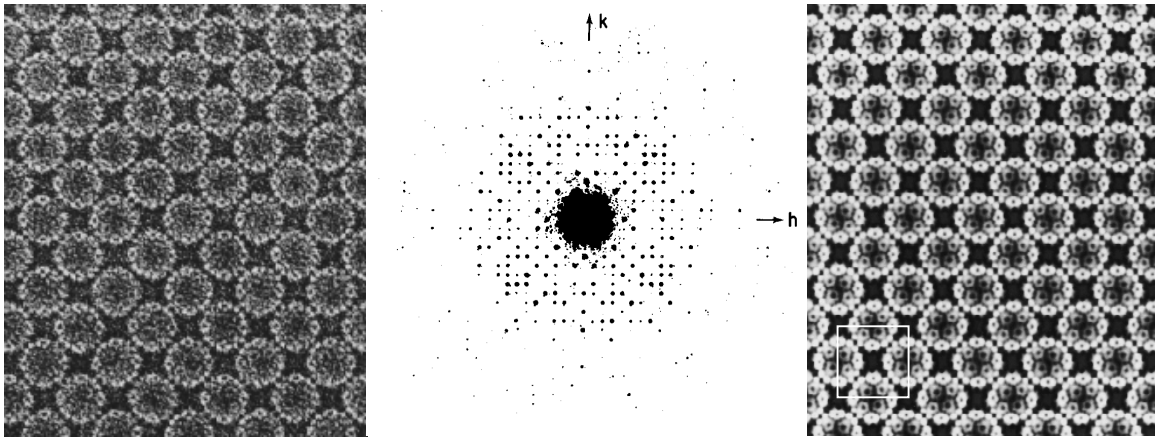

Fig. III.90. Fourier averaging of a negatively stained crystal of cowpea chlorotic mottle virus (CCMV). (Left) Image of a small portion of a CCMV 2D crystal. (Center) Optical diffraction pattern of small region of CCMV crystal exhibits pseudo tetragonal symmetry (p4) with a=b=375Å. The true unit cell is $p2_12_1$ as exhibited by the phase relationships in the Bragg reflections (see Fig. III.91). (Right) Grey level display of the Fourier averaged image of the CCMV crystal, with $p2_12_1$ symmetry imposed. The unit cell (white box) contains two virus particles, related to each other by a rotation of ~86°.

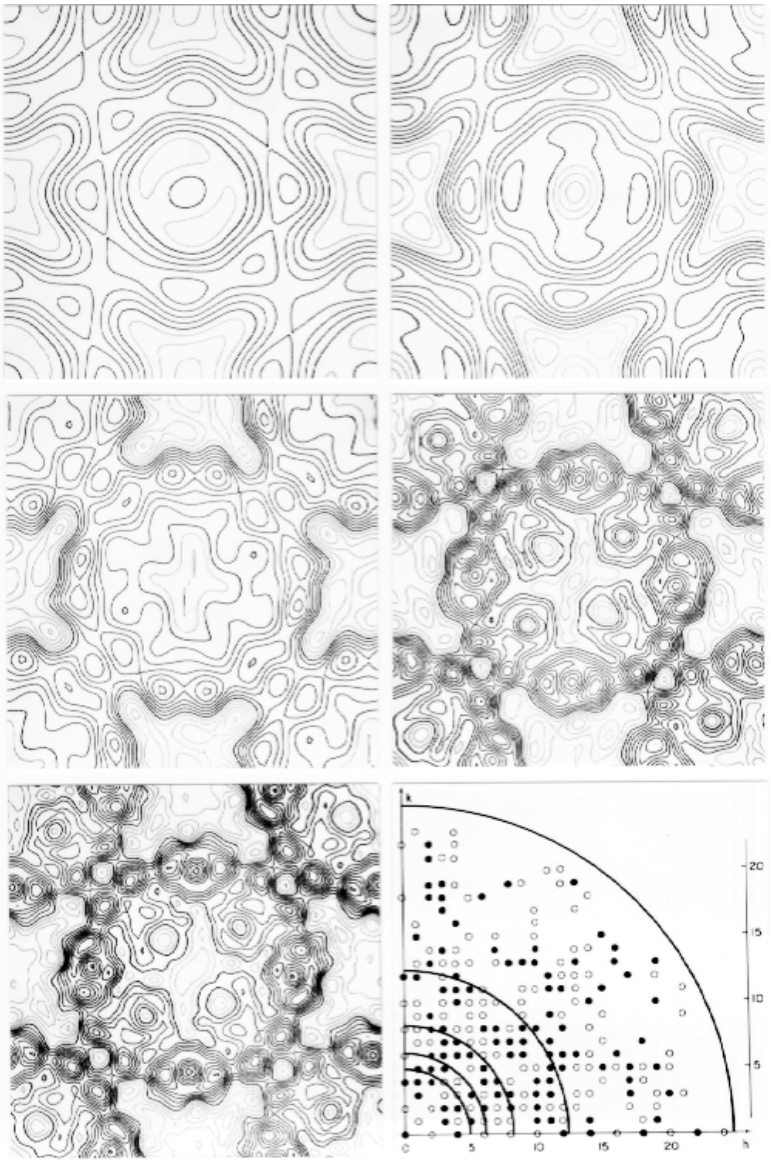

Fig. III.91. Fourier average of CCMV at increasing resolution limits. Five contoured views of a single CCMV particle from the Fourier average shown in Fig. III.90, are displayed at progressively higher resolutions, from 75Å (top left) to 60 (top right) to 45 and 30Å (middle panels) to 15Å (bottom left). In each contour display, the darker lines outline the stain excluding regions and the lighter lines outline the negative stain. (Bottom right) A representation of one quarter of the CCMV transform, with large circles indicting the resolution limits imposed to produce the displays in the other panels and open and closed small circles indicate the phases (0 or 180°, respectively) of each of the observed Bragg reflections. The phases obey the relationships required by plane group $p2_12_1$. Also, note the systematic absences along the *h* and *k* directions of the diffraction pattern.

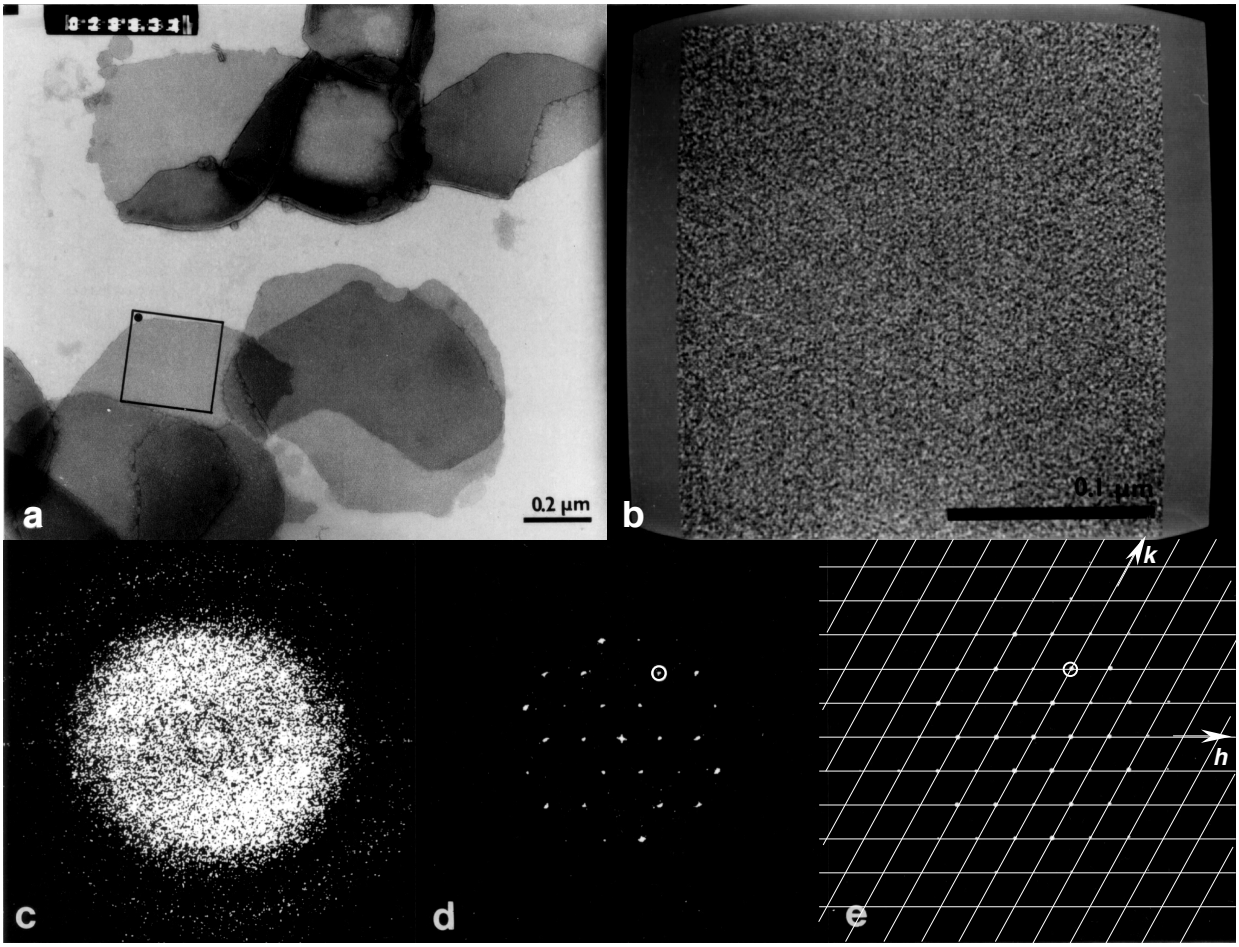

SPOT 0 2

AMPLITUDES

5	10	7	11	5	4	10	5	6
6	6	21	9	3	8	1	13	9
4	14	8	8	5	3	1	5	1
9	16	15	7	8	11	7	4	5
9	14	19	10	85	18	25	14	10
10	10	13	15	46	27	15	18	7
8	6	7	7	12	6	14	10	6
9	5	6	6	21	16	8	3	6
6	3	5	7	15	13	4	13	5

PHASES

3	30	24	31	36	31	31	6	23
33	18	10	9	31	7	9	9	10
29	3	5	7	5	29	14	16	25
28	1	4	1	13	14	2	21	20
7	26	3	17	23	25	4	24	16
1	20	30	15	23	31	9	25	33
30	34	35	7	7	18	20	32	2
10	2	31	28	22	24	34	25	16
29	17	26	25	13	12	17	19	32

AMP = 5598.3 PHASE = 232.3

BACK = 1333.2 CALCULATED CENTER AT -0.03, -0.39

f g

Fig. III.92. Fourier averaging of image of negatively stained gap junction membrane. (a) Low magnification view of entire micrograph shows several stained gap junction membranes. The area outlined with the square black box was digitized and displayed on a raster graphics device. In some regions, two or three junction membranes lie stacked above one another on the EM grid. (b) Display of region boxed and floated from the original micrograph shown in (a). (c) Computer graphics display of the intensities in the Fourier transform of (b), with the transform scaled to reveal the contrast transfer function of the microscope. Note the slight astigmatism revealed in the non-circular noise pattern. (d) Same as (c) but scaled to show just the most intense peaks in the transform. The *h,k=0,2* Bragg reflection is encircled. (e) Same as (d) with a reciprocal lattice overlay. (f) Structure factor amplitudes (on left) and phases (on right) extracted from the 512^2 transform for the region centered about the *h,k=0,2* reflection circled in (d,e). Each phase value is divided by 10 (*e.g.* a phase of 23 at the center actually represents a phase of 230°). A single structure factor amplitude (5598.3) is integrated from within a circle like the one depicted, centered at position -0.03 in *x* and -0.39 in *y*, with respect to the grid point in the center of each window of data points (amp=85, phase=23). The single structure factor phase (232.3°) is calculated by interpolation from the four data points closest to the calculated center of the 0,2 spot. (g) Fourier average computed by back transformation of the set of structure factors extracted as shown in (f).

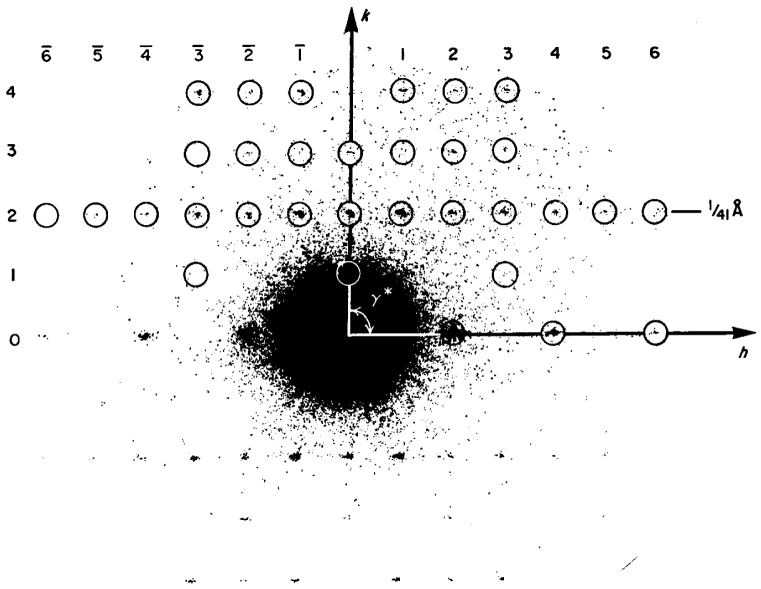

Fig. III.93. Indexed, optical diffraction pattern of Zn tubulin sheets, which were negatively stained with uranyl acetate. This image was recorded under minimal dose conditions (~20e$^-$/Å^2). The equatorial and meridional axes are labeled *h* and *k,* respectively. The intensity distribution obeys a near perfect *mm* relationship (i.e. each spot has two mirror-related mates reflected across the *h* and *k* mirror lines. Measurement of the a* and b* dimensions in the orthogonal reciprocal lattice indicates an orthogonal (rectangular) unit cell with a=97Å, b=82Å, and γ=90°. Systematic absences along the *h* direction reveal the presence of a 2_1 screw axis parallel to the *a* cell direction. (From Baker and Amos, 1978, p.96)

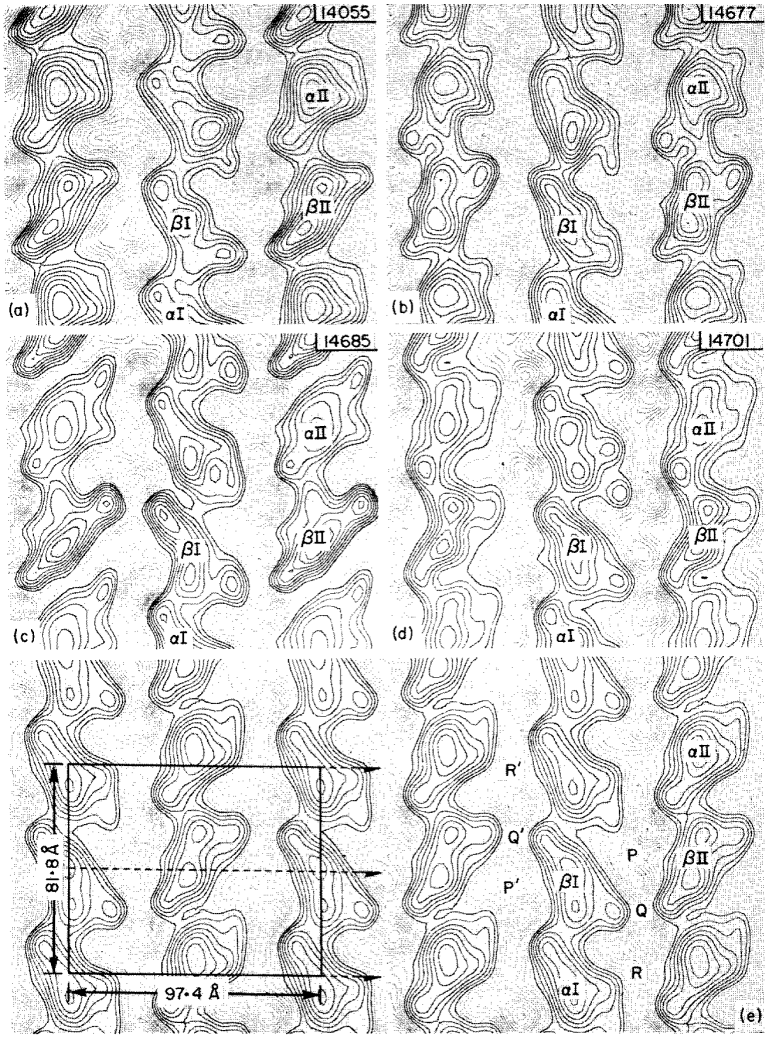

Fig. III.94. Image reconstructions of four individual Zn tubulin sheets and their average (bottom panel). Dark lines represent contours of density from zero to successively higher positive amplitudes. Light lines represent contours at negative amplitudes. (a-d) Individual reconstructions from four images, showing corresponding regions of the structure. Subunits are labeled to indicate possible pairing of monomers into heterodimers, and to show the relationship of dimers in adjacent protofilaments. The α and β labels are arbitrary. (e) Average reconstruction of the four sheets (a) to (d), showing contents of several unit cells. One cell is outlined, and the positions of the dyad screw axes are indicated by broken lines with half arrows. Note, however, that NONE of these reconstructions have had a perfect screw axis symmetry enforced. (From Baker and Amos, 1978, p.99)

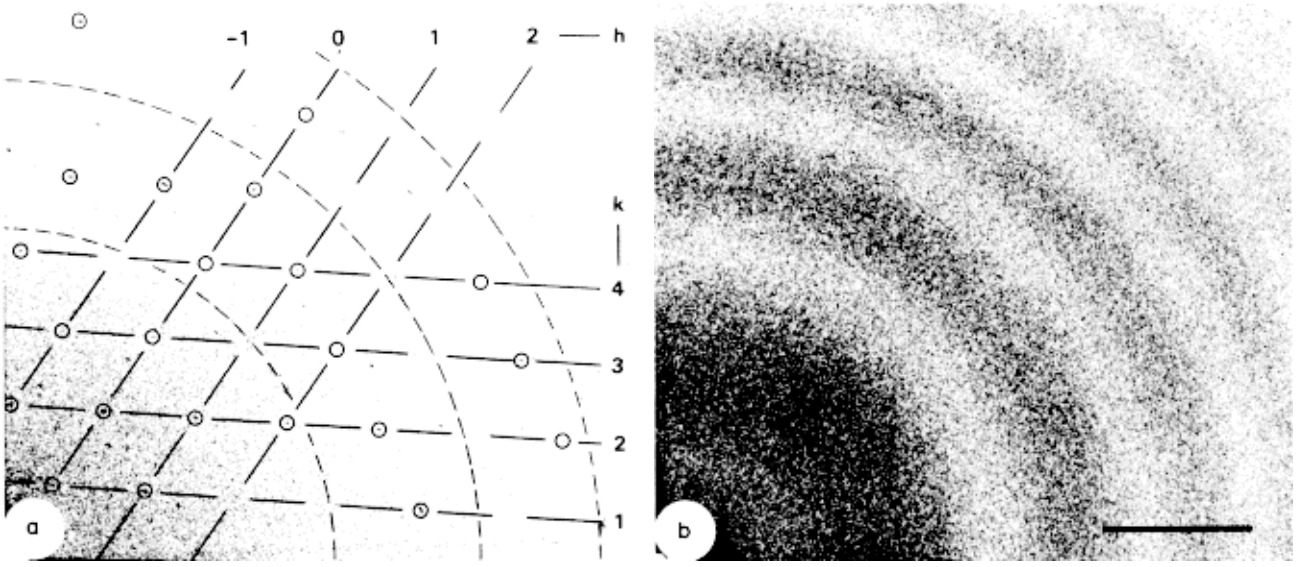

Fig. III.95. Upper right quadrants from optical transforms of unstained purple membrane micrographs recorded by bright-field TEM: (a) Optical transform from low dose image, (b) Optical transform from high dose image. Diffraction bar = 1/33Å. (From Misell, 1978, p.174; adapted from Unwin and Henderson, 1975)

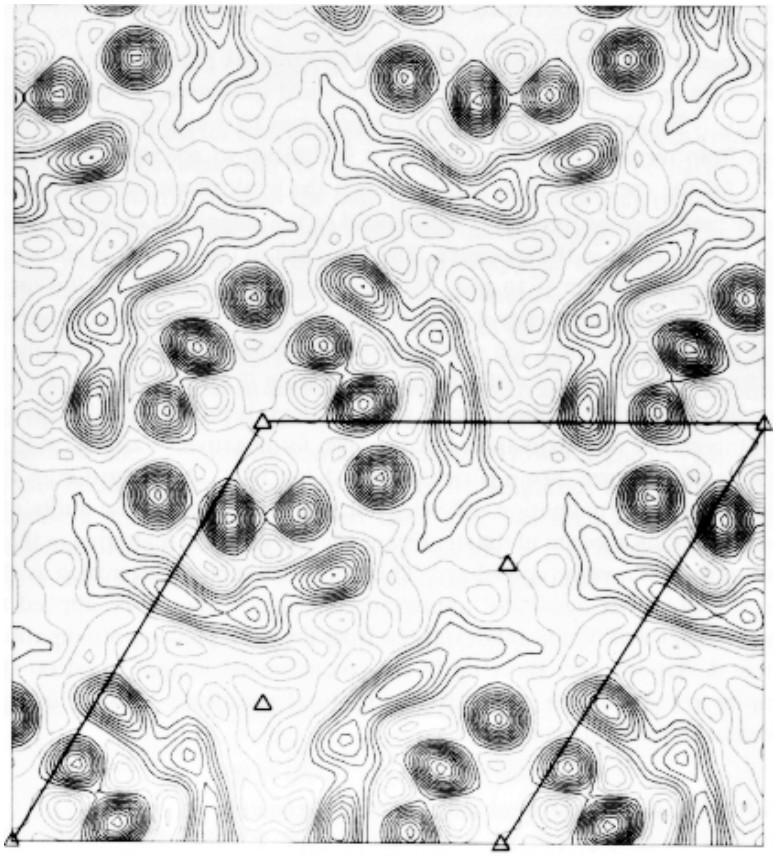

Fig. III.96. Contour map of the projected structure of purple membrane at 7Å resolution. Thicker lines show positive contours; positive peaks arise from higher concentrations of scattering material (protein) relative to surrounding regions. Low density regions indicated by thinner lines are due to lipid and glucose. Unit cell dimensions are 62Å x 62Å. (From Misell, 1978, p.175; adapted from Unwin and Henderson, 1975)

b. 2D averaging of objects with point group symmetry: rotational filtering

Specimens that only possess rotational symmetry, such as individual oligomeric proteins, spherical viruses, and bacteriophage baseplates (Fig. III.97), have been studied by several image processing methods. These include 2D rotational photographic-superposition and 2D digital rotational filtering, and 3D reconstruction. In this section, only the 2D averaging methods are discussed. Digital, rotational filtering and photographic superposition techniques produce *qualitatively* similar results, but the photographic methods should be used with caution and usually with specimens displaying obvious or well-established symmetry. Crowther and Amos (1971) and Misell (1978) compare the real-space and Fourier-space methods.

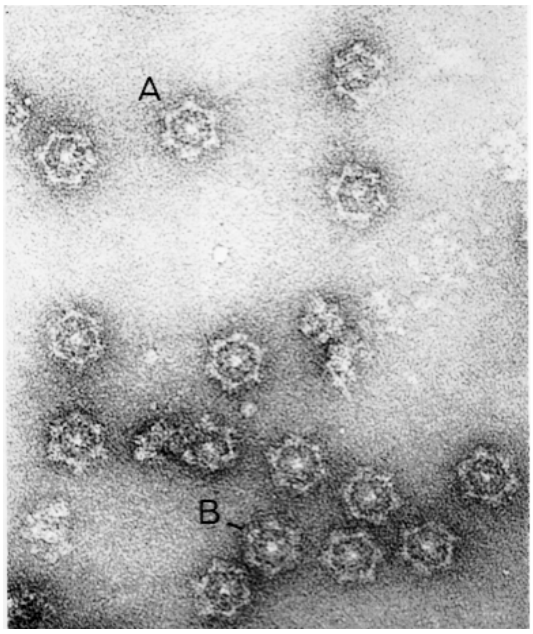

Fig. III.97 A negatively stained preparation of base plates from bacteriophage T4. Rotationally filtered images of particles A and B are shown in Fig. III.102. (From Crowther and Amos, 1971, Plate I)

1) Rotational photographic superposition method

Markham *et al.* (1963) devised a simple, real-space method for analyzing images of particles with rotational symmetry. The basic apparatus used consists of a photographic enlarger and a movable board to which a card is attached that can be rotated about an axis (Fig. III.98). The specimen image is projected onto a photographic print attached to the card and a series of *n* images are exposed onto the print, with the print rotated by *360°/n* after each of *n* exposures. For example, if the object of interest had 6-fold rotational symmetry, and a normal, straight photographic print required a 12 second exposure, then a total of six, two-second exposures would be required to produce the rotational superposition photographic image. Presumably, *maximum* reinforcement of detail is given when *n* is the true periodicity in the image of the object. This also presumes, of course, that the rotation axis of the print can be positioned accurately at the center of symmetry in the image. If they do *not* coincide, the true symmetry of the object may be missed and details will certainly get smeared out in the reconstruction. Thus, the correct centering of the photographic print with respect to the rotational symmetry axis in the image and the correct choice of *n* are important components in successful application of this method. A mistake in either choice leads to erroneous results.

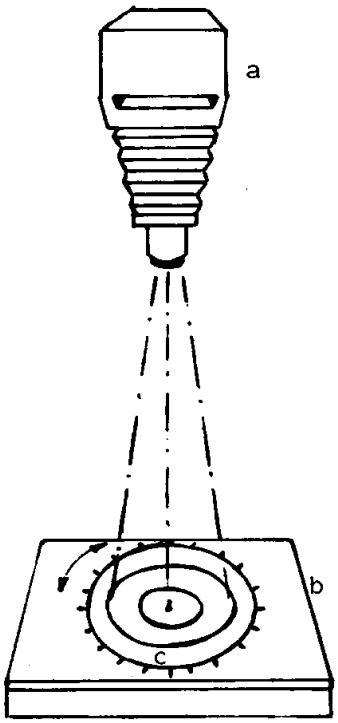

Fig. III.98. Apparatus for photographically integrating detail in micrographs with radial symmetry. (a) Enlarger unit containing micrograph with region to be studied accurately centered in relation to the lens. (b) Movable board containing rotary disc. (c) The center of rotation must be carefully aligned to the selected region of the micrograph shown at (a). (From Horne and Markham, 1972, p.413)

The main disadvantage of the optical superposition method is that it requires a visual assessment step, which may be more influenced, by what is eye-catching rather than what is correct. The computational, rotational filtering method described in the next section provides quantitative information in the form of the rotational power spectrum. The rotational power spectrum allows quantitative assessment of the presence of a particular rotational symmetry. Once the symmetry is known, a filtered image can be resynthesized from only

those components that obey the chosen rotational symmetry.

A second type of apparatus for producing rotationally symmetrized images by the photographic superposition method is shown below (Fig. III.99).

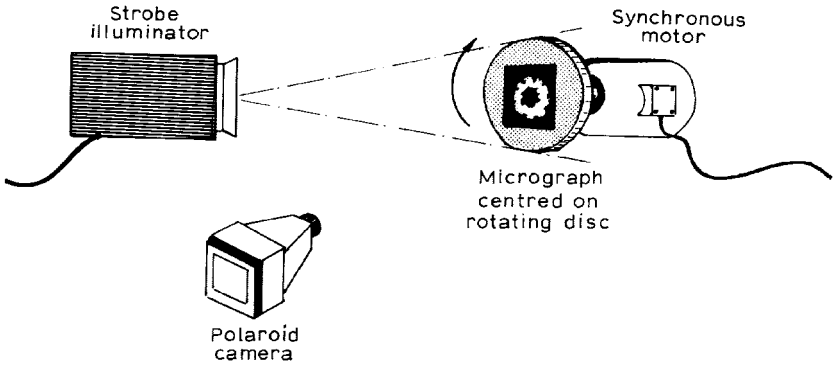

Fig. III.99. The arrangement of an apparatus for analyzing electron micrographs by rotational integration with the aid of a strobe illuminator. (From Horne and Markham, 1972, p.415)

2) 2D digital processing of rotationally symmetric particles- Power spectrum and rotational filtering analysis

Conversion from Cartesian to Polar Form

The digitization, boxing, and floating of the specimen image is performed as usual and subsequent computations are conveniently performed in polar coordinates (r,ϕ) (Fig. III.100). Thus, a Cartesian image, $\rho(x,y)$, is converted to a polar image, $\rho(r,\phi)$, by subdividing the Cartesian image into a series of equally spaced annuli (Fig. III.101) and interpolating the densities within each annulus. The polar density function can be expanded into a series of circular waves much as a Cartesian image is conveniently expanded into a series of plane waves (Fig. III.101).

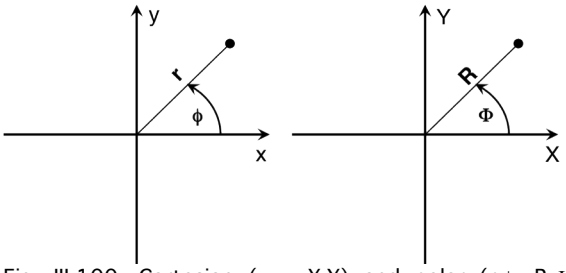

Fig. III.100. Cartesian (x,y; X,Y) and polar (r,ϕ; R,Φ) coordinate systems in real (left) and reciprocal (right) space.

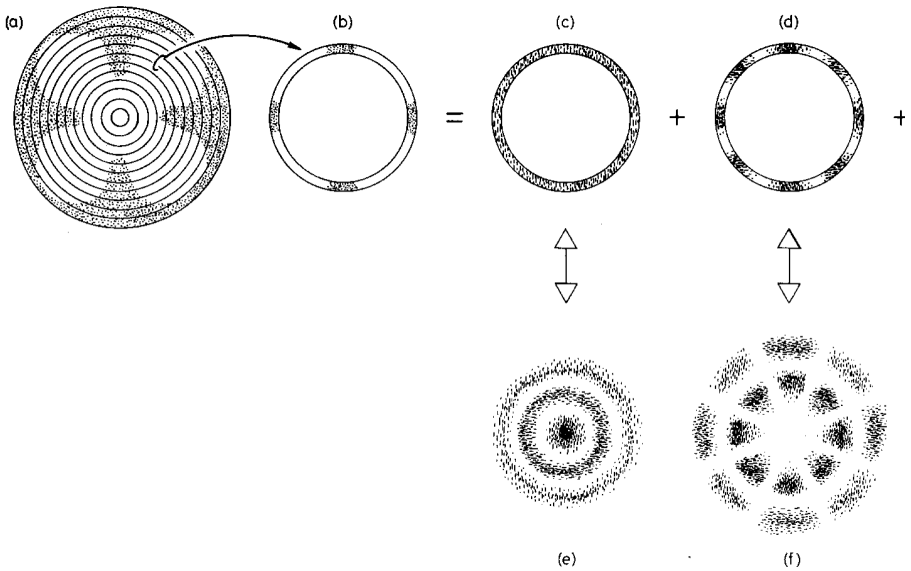

Fig. III.101. The Fourier method for finding rotational symmetry. The image (a) is divided into a series of concentric, equal-spaced annuli, of which one (b) is expressed as the sum of two of its rotational Fourier components ((c), the zero-fold and (d) the eight-fold symmetric component). The Fourier transforms of (c) and (d) are shown in (e) and (f), respectively. (From Moody, 1990, p.239)

$$\rho(r,\phi) = \sum_{n=-\infty}^{\infty} g_n(r) e^{in\phi} \tag{1}$$

In equation (1), each $g_n(r)$ represents the weight of the n-fold azimuthal component of the image at a radius *r*. The phase term, $\exp(in\phi)$, positions the peak of each circular wave with respect to an origin (usually the *x* axis) so that all $g_n(r)$ are properly summed.

Rotational Power Spectrum

Each $g_n(r)$ is integrated over the radius of the particle, *a*, to obtain a measure of the total n-fold rotational component of the image. Power in the image is defined as:

$$P_n = \varepsilon_n \int_0^a |g_n(r)|^2 2\pi r dr, \qquad \varepsilon_n = \begin{cases} 1 \text{ for } n = 0 \\ 2 \text{ for } n > 0 \end{cases} \tag{2}$$

$\varepsilon_n = 2$ accounts for the fact that P_n has equal contributions from g_n and g_{-n} for n>0.

The rotational power spectrum is a plot of P_n as a function of *n*. This is a compact way to represent the rotational symmetry components in the image. P_0 is usually normalized to 1.0 and the spectrum is displayed with the P_n on a logarithmic scale (Figs. III.102 and III.103).

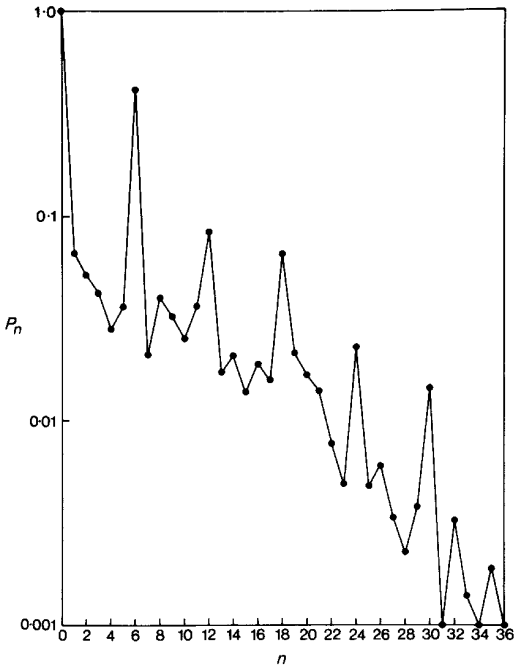

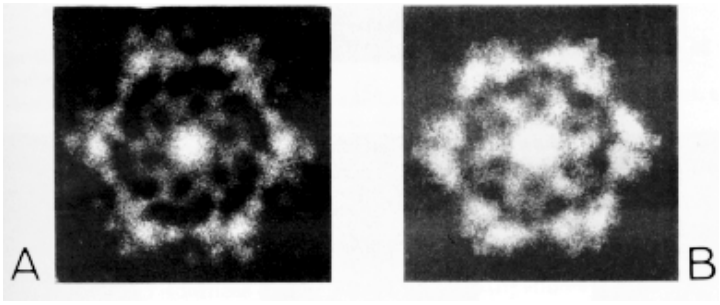

Fig. III.102. (Left) A logarithmic plot of the rotational power spectrum of a T4 bacteriophage base plate (particle A in Fig. III.97), showing the strong 6-fold symmetry of the image. The curve is normalized with P_0 = 1 and the power associated with rotational frequencies higher than n = 36 is less than 0.001. (From Crowther and Amos, 1971, Fig.2, p.126). (Top) 6-fold rotationally symmetrized images of negatively stained base plates from bacteriophage T4 (particles labeled A and B in Fig. III.97). The two filtered images have rather different appearances because they have been plotted at different density levels, but the main features of each are very similar. (From Crowther and Amos, 1971, Plate I)

3) Fourier Bessel Transform

As with other types of specimens, it is convenient with rotationally symmetric specimens to perform computations in Fourier space rather than real space. The polar Fourier transform coordinates are *R* and Φ. The transform is expanded in the following way:

$$F(R,\Phi) = \sum_{n=-\infty}^{n=+\infty} \int_0^a g_n(r) J_n(2\pi r R) e^{in(\Phi+\pi/2)} 2\pi r dr \tag{3}$$

$$= \sum_{n=-\infty}^{n=+\infty} G_n(R) e^{in(\Phi+\pi/2)} \tag{4}$$

$J_n(X)$ is a Bessel function of order *n*. Each J_n is a circularly symmetric, oscillatory function (Fig.

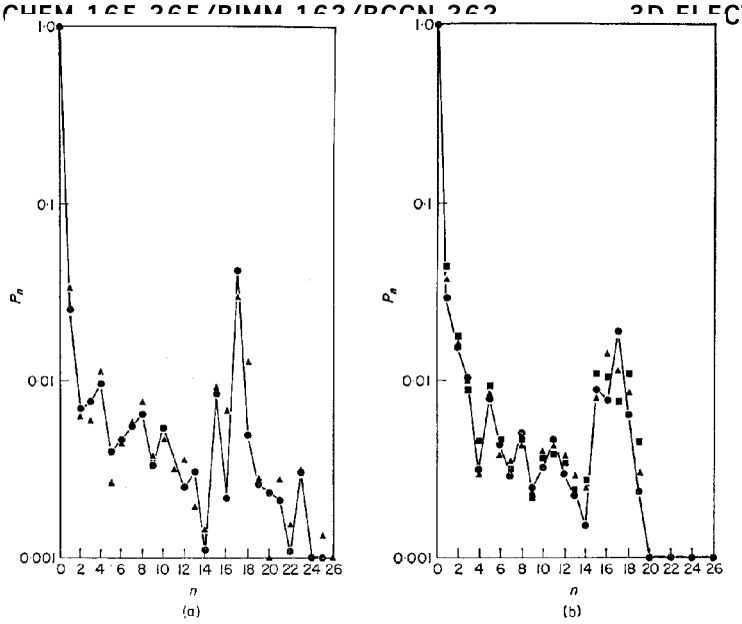

Fig. III.103. Logarithmic plots of the rotational power spectra of two images of discs of tobacco mosaic virus protein. (a) A well-preserved disc (Fig. III.109(a)) in which no one component is dominant. In each case the solid curve (-●-) refers to a choice of origin that maximizes the 17-fold component. In (a) the triangles (▲) refer to a choice of origin which simultaneously maximizes the 16- and 18-fold components, while in (b) the triangles (▲) and squares (■) refer to choices of origin which maximize respectively the 16- and 18-fold components. The curves are normalized with P_O = 1 and the power associated with rotational frequencies higher than n = 26 is less than 0.001. (From Crowther and Amos, 1971, p.127)

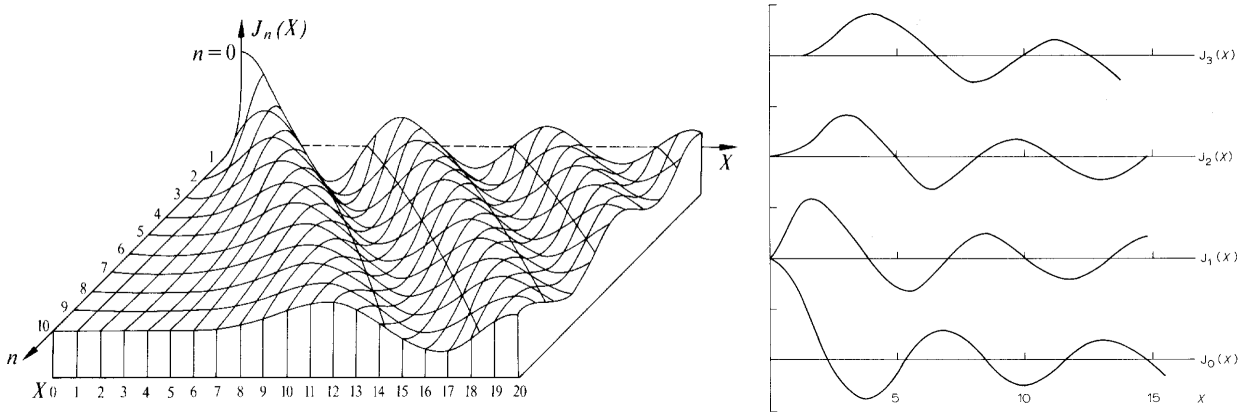

Fig. III.104. (Left) The behavior of the Bessel function $J_n(X)$ for various values of n. (From Sherwood, 1976, p. 565). (Right) Amplitude variations of the Bessel function $J_n(X)$ for n = 0 to 3. (From Misell, 1978, p.98)

III.104). The first maximum of $J_n(X)$ for large n (*i.e.* n > about 5) appears at about X = n+2.

The transform of a ring of radius a is given by $2\pi aJ_0(2\pi aR)$ (Fig. III.105). Such a ring can be considered to be generated from a pair of points, separated by the distance $2a$ that are rotated through the angle π. A single pair of points at opposite sides of a circle gives rise to cosine fringes. When rotationally averaged, the fringes reinforce at the origin but tend to cancel away from the origin. This gives rise to a Bessel function of zero order (J_0).

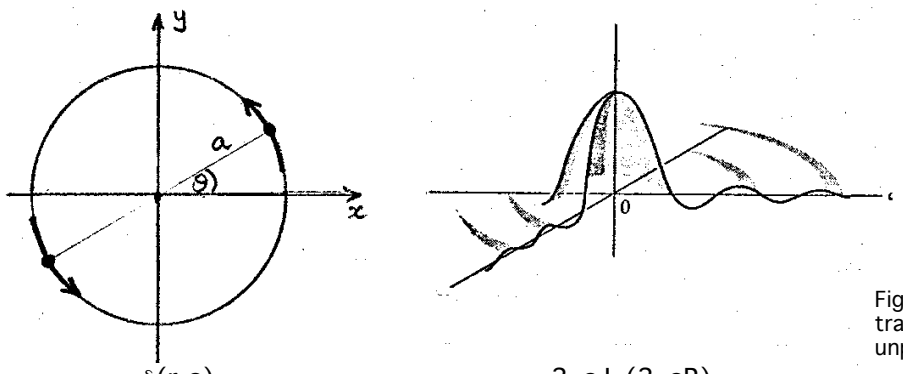

Fig. III.105. A ring (left) and its transform (right). (Taken from Crowther unpublished course notes, 1973)

The expansion of the Fourier Transform (equation 4) is analogous to the expansion of the polar image densities as given in equation (1). Thus, the $G_n(R)$ are the coefficients (weights) of each azimuthal component in the Fourier transform. The two sets of coefficients, $G_n(R)$ and $g_n(r)$, are connected by what is called the Fourier-Bessel transform.

$$g_n(r) = \int_0^\infty G_n(R) J_n(2\pi R r) 2\pi R\, dR \tag{5}$$

In practice, the above integral would normally only be evaluated out to some resolution limit (*i.e.* with $R < \infty$).

The inverse relationship also holds:

$$G_n(R) = \int_0^a g_n(r) J_n(2\pi r R) 2\pi r\, dr \tag{6}$$

where r_0 is the radial limit of the object.

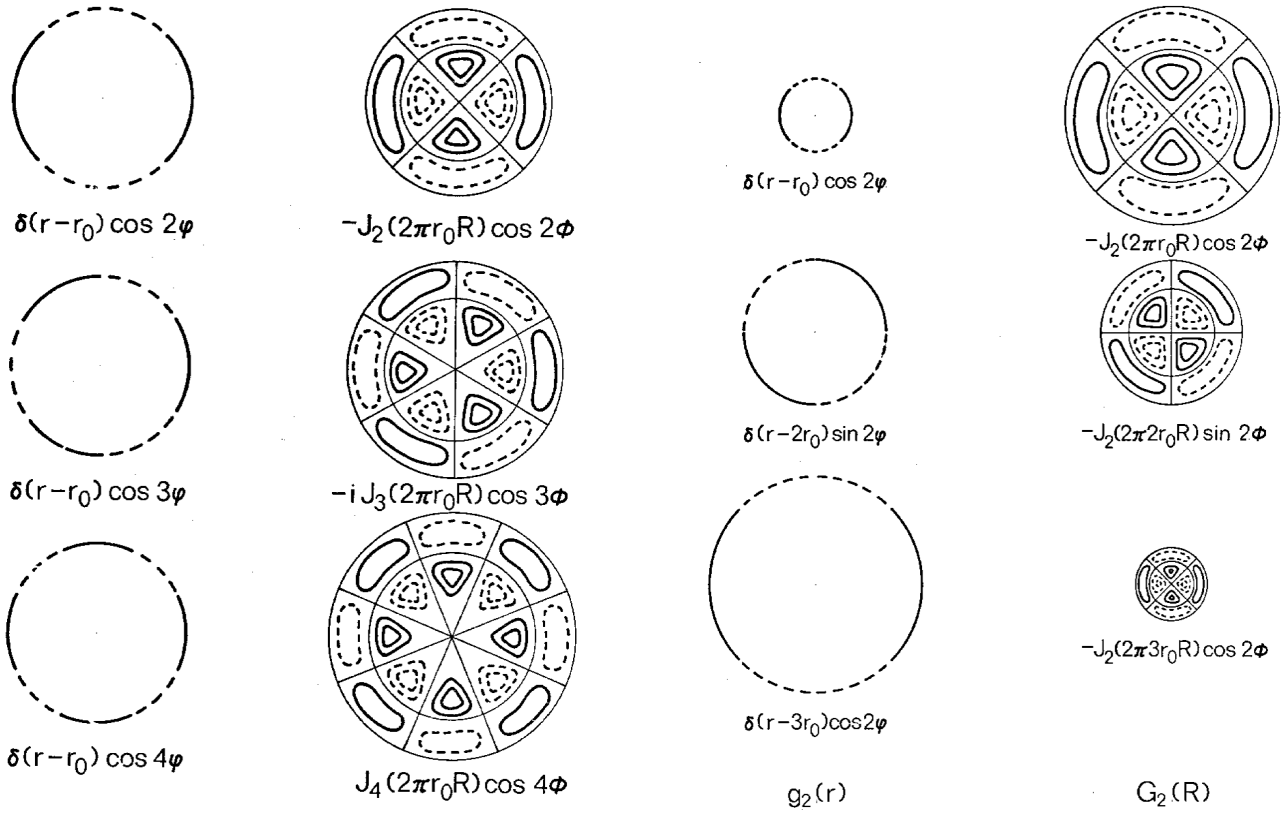

Fig. III.106. (Left two columns) Density functions with 2-, 3-, and 4-fold azimuthal variations and the corresponding Fourier-Bessel transforms. (Right two columns) Two-fold azimuthal density functions of different radii and orientation and the respective Fourier-Bessel transforms. (Taken from Crowther unpublished course notes, 1973)

Examples of the relationship between objects with *n*-fold sinusoidal variations in azimuth ($g_n(r)$) and the corresponding Fourier-Bessel transforms ($G_n(R)$) are illustrated in Figs. III.106 and III.107.

4) Phase Origin

It is **essential** that the origin of the polar coordinate system lie **on** the symmetry axis of the particle image. Initially, the origin chosen by eye during the boxing procedure necessarily becomes the phase origin of the Fourier transform. The origin point is then shifted to get the best P_n for the assumed symmetry (Fig. III.108). By changing the assumed symmetry, *m*, one gets a series of origins and computes for each of these separate origins a series of rotational power spectra. These are compared to look for the dominant symmetry.

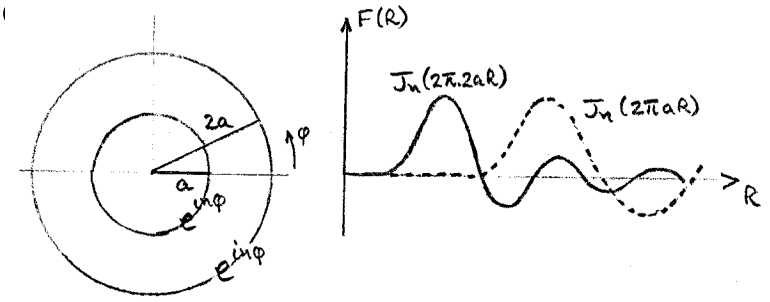

Fig. III.107. An object consisting of two rings of radii *a* and 2*a*, each with an *n*-fold azimuthal variation (left) gives rise to overlapping Bessel functions which tend to cancel apart from their major peaks (right). (Taken from Crowther unpublished course notes, 1973)

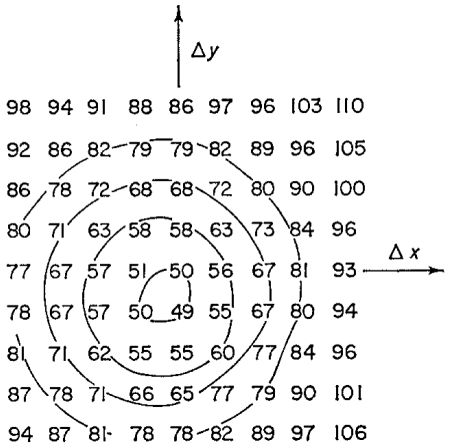

Fig. III.108. A plot of the residual function obtained when determining the best position for the origin of a T4 bacteriophage base plate (particle A, Fig. III.97), based on an assumed 6-fold symmetry. The origin is shifted by steps Δx, Δy of approximately 2.5 Å from the initial approximate position chosen by eye. For a particle with perfect 6-fold symmetry the residual should be zero when the origin coincides with the 6-fold axis. It is the sharpness of the minimum that is important for accurate determination of the position of the origin, and it can be seen that, in this case, the residual approximately doubles for a shift of origin of about 10 Å from the position corresponding to the minimum. (From Crowther and Amos, 1971, p.125)

5) Synthesis of filtered image

One typically examines the rotational power spectra computed from several different particle images to get an idea of the relative preservation of the particles. Those images that show the highest P_n are used to synthesize rotationally filtered images. Equation (5) is used to convert each G_n to a corresponding g_n and only those g_n for which n is a multiple of m are computed, thereby omitting all other components considered to be noise. Noise may arise from several sources such as:

1) The particle may not be viewed **directly** along an axis of symmetry

2) The particle may be distorted or may be non-uniformly stained, shadowed, etc.

3) The other usual forms of noise (*e.g.* support film, electron optical effects, etc.) may be present.

The $G_n(R)$ are computed from the Fourier transform by the inverse of equation (4):

$$G_n(R) = \frac{1}{2\pi}\int_0^{2\pi} F(R,\Phi)\, e^{-in(\Phi+\pi/2)}\, d\Phi \qquad (7)$$

In using equation (5) to compute the $g_n(r)$, n is set to some limit since P_n is effectively zero beyond certain n (resolution limit). The highest value used for n, thus limits the fineness of detail that can be seen in the reconstructed image.

Note that the computation of $G_n(R)$ from $F(R,\Phi)$ (equation 7) allows the P_n to be computed either from densities directly (equation 2) or from the Fourier transform as follows:

$$P_n = \varepsilon_n \int_0^{R_{max}} |G_n(R)|^2\, 2\pi R dR \qquad (8)$$

Once the $g_n(r)$ are computed, equation (1) is used to resynthesize the density function, $\rho(r,\phi)$. This polar image is then reconverted back to a Cartesian format, $\rho(x,y)$, and displayed (*e.g.* Figs. III.102, III.109, and III.110).

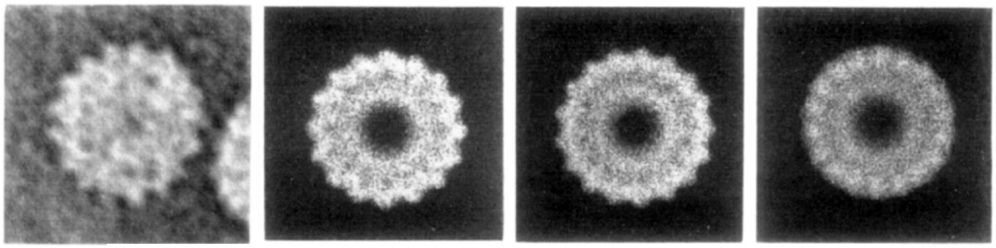

Fig. III.110. (a) Image of a negatively stained disc of tobacco mosaic virus protein. This is a poorly preserved particle as judged by the rotational power spectrum (Fig. III.103(b)). (b), (c), and (d) show respectively the results of 16-, 17- and 18-fold filtering. 16-fold filtering produces the most eye-catching image, although it is not the strongest harmonic. (From Crowther and Amos, 1971, Plate III)

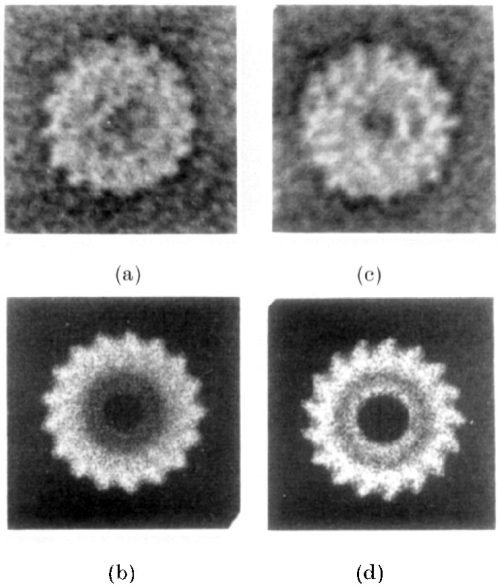

Fig. III.109. (a) and (c) Images of negatively stained discs of tobacco mosaic virus protein. (b) and (d) Results of 17-fold filtering of the images shown in (a) and (c), respectively. These images are well preserved as judged by the dominance of a single rotational symmetry in the power spectrum (Fig. III.103(a)). Note that the two filtered images, which have been processed in an identical manner, are of opposite hand, thus confirming the polar nature of the disc. The density level in plotting has been chosen to be rather high in order to emphasize the azimuthally varying component, thereby accentuating the hole at center of the particle. (From Crowther and Amos, 1971, Plate II)

6) Comparison of Numerical and Photographic Superposition Methods

Recall the analogy of optical filtering and translational photographic superposition with crystalline (translationally symmetric) specimens (§ III.D.2.g). The optical diffraction pattern of such a specimen is basically a translational power spectrum of the specimen image. This diffraction pattern makes possible the objective analysis of the periodicities and preservation of the object's translational symmetry.

It is not possible to perform optical filtering of rotationally symmetric objects because the wanted and unwanted Fourier components are not spatially separated in the diffraction plane. Thus, it is necessary to compute the power spectrum and filter the image numerically. This procedure, like with translationally-symmetric specimens, involves two steps:

1. Analysis (Fourier analysis) to separate the image into Fourier components.

2. Synthesis (Fourier synthesis) to recombine just those components that satisfy the symmetry.

Photographic superposition methods attempt to determine the symmetry **AND** produce an average **at the same time**. The digital filtering approach is more reliable and powerful because of the separation of these two steps. An additional benefit of the digital processing procedure is that it provides quantitative assessment. Other advantages are that more complex operations can be performed on numerical data (*e.g.* CTF corrections), and it is a relatively straightforward procedure to combine data from a number of different images and compute difference images.

III.D.5. References Cited in §III.D.

Aebi, U., P. R. Smith, J. Dubochet, C. Henry, and E. Kellenberger (1973) A study of the structure of the T-layer of Bacillus brevius. *J. Supra. Struct.* **1:498-522.**

Arndt, U. W., J. B. Leigh, J. F. W. Mallett, and K. E. Twinn (1969) A mechanical microdensitometer. *J. Phys. E: Sci. Instrum.* **2:385-387.**

Baker, T. S. (1981) Image processing of biological specimens: a bibliography, pp. 189-290, Chap. 6 *In* J. D. Griffith, Ed., Electron Microscopy in Biology. Vol. 1, John Wiley and Sons, New York.

Baker, T. S. and Amos, L. A. (1978) Structure of the tubulin dimer in zinc-induced sheets. *J. Mol. Biol.* **123:89-106.**

Bancroft, J. B., G. J. Hills, and R. Markham (1967) A study of the self-assembly process in a small spherical virus: formation of organized structures from protein subunits in vitro. *Virology* **31:354-379.**

Baxter, W. T., A. Leith, and J. Frank (2007) SPIRE: the SPIDER reconstruction engine. *J. Struct. Biol.* **157:56-63.**

Berger, J. E., C. A. Taylor, D. Shechtman, and H. Lipson (1972) Miscellaneous applications, pp. 401-422, *In* H. Lipson, Ed., Optical Transforms. Academic Press, London.

Blundell, T. L. and L. N. Johnson (1976) Protein Crystallography, p. 565, Academic Press, N. Y.

Bragg, W. L. (1939) A new type of 'X-ray microscope'. *Nature* **143:678.**

Crowther, R. A. and Amos, L. A. (1971) Harmonic analysis of electron microscope images with rotational symmetry *J. Mol. Biol.* **60:123-130.**

DeRosier, D. J. and A. Klug (1972) Structure of the tubular variants of the head of bacteriophage T4 (polyheads). I. Arrangement of subunits in some classes of polyheads. *J. Mol. Biol.* **65:469-488.**

DeRosier, D. J. and P. B. Moore (1970) Reconstruction of three-dimensional images from electron micrographs of structures with helical symmetry. *J. Mol. Biol.* **52:355-369.**

Erickson, H. P., W. A. Voter, and K. Leonard (1978) Image reconstruction in electron microscopy: enhancement of periodic structure by optical filtering. *Methods in Enzym.* **49:39-63.**

Finch, J. T., A. Klug, and M. V. Nermut (1967) The structure of the macromolecular units on the cell walls of Bacillus polymyxa. *J. Cell Science* **2:587-590.**

Fraser, R. D. B. and Millward, G. R. (1970) Image averaging by optical filtering. *J. Ultrastruc. Res.* **31:203-211.**

Haydon, G. B. and D. J. Scales (1973) Pitfalls in optical filtering techniques. *In* Elec. Microsc. Soc. Am. Proc. **31:276-277.**

Horne, R. W. and R. Markham (1972) Application of optical diffraction and image reconstruction techniques to electron micrographs, pp. 327-440, *In* A. M. Glauert, Ed., Pract. Meth. Elec. Microsc. Vol. 1, North-Holland Pub. Co, Amsterdam.

Johansen, B. V. (1975) Optical diffractometry, pp. 114-173, *In* M. A. Hayat, Ed., Princ. Tech. Elec. Microsc. Vol. 5, Van Nostrand Reinhold Co., New York.

Kiselev, N. A. and A. Klug (1969) The structure of viruses of the papilloma-polyoma type V. Tubular variants built of pentamers. *J. Mol. Biol.* **40:155-171.**

Kiselev, N. A., F. Y. Lerner, and N. B. Livanova (1971) Electron microscopy of muscle phosphorylase b. *J. Mol. Biol.* **62:537-549.**

Klug, A. and J. E. Berger (1964) An optical method for the analysis of periodicities in electron micrographs, and some observations on the mechanism of negative staining. *J. Mol. Biol.* **10:565-569.**

Klug, A. and D. J. DeRosier (1966) Optical filtering of electron micrographs: reconstruction of one-sided images. *Nature* **212:29-32.**

Lake, J. A. (1972) Biological studies, pp. 153-188, *In* H. Lipson, Ed., Optical Transforms. Academic Press, London.

Leonard, K. R., A. K. Kleinschmidt, and J. A. Lake (1973) Caulobacter crescentus bacteriophage ϕ-CbK: structure and in vitro self-assembly of the tail. *J. Mol. Biol.* **81:349-365.**

Markham, R., S. Frey, and G. J. Hills (1963) Methods for the enhancement of image detail and accentuation of structure in electron microscopy. *Virology* **20:88-102.**

Markham, R., J. H. Hitchborn, G. J. Hills, and S. Frey (1964) The anatomy of the tobacco mosaic virus. *Virology* **22:342-359.**

Misell, D. L. (1978) Image analysis, enhancement and interpretation, pp. 1-305, *In* A. M. Glauert, Ed., Pract. Meth. Elec. Microsc. Vol. 7, North-Holland Pub. Co., Amsterdam.

Moody, M. F. (1967) Structure of the sheath of bacteriophage T4. I. Structure of the contracted sheath and polysheath (Appendix: the interpretation of optical diffraction patterns of electron micrographs of negatively stained helical structures). *J. Mol. Biol.* **25:167-200.**

Moody, M. F. (1990) Image analysis of electron micrographs, pp. 145-287, Chap. 7 *In* P. W. Hawkes and U. Valdre, Eds., Biophysical Electron Microscopy: Basic Concepts and Modern Techniques. Academic Press Limited, London.

Mulvey, T. (1973) Instrumental aspects of image analysis in the electron microscope. *J. Microsc.* **98:232-250.**

Sherwood, D. (1976) Crystals, X-rays and Proteins, p. 702, John Wiley & Sons, New York.

Slayter, E. M. (1970) Optical Methods in Biology, p. 757, John Wiley & Sons, New York.

Steven, A. C., E. Couture, U. Aebi, and M. K. Showe (1976) Structure of T4 polyheads. II. Pathway of polyhead transformations as a model for T4 capsid maturation. *J. Mol. Biol.* **106:187-221.**

Tang, G., L. Peng, P. R. Baldwin, D. S. Mann, W. Jiang, I. Rees, and S. J. Ludtke (2007) EMAN2: an extensible image processing suite for electron microscopy. *J. Struct. Biol.* **157:38-46.**

Taylor, C. A. and J. K. Ranniko (1974) Problems in the use of selective optical spatial filtering to obtain enhanced information from electron micrographs. *J. Microsc.* **100:307-314.**

Thompson, B. J. (1972) Coherence requirements, pp. 27-69, *In* H. Lipson, Ed., Optical Transforms. Academic Press, London.

Unwin, P. N. T. and R. Henderson (1975) Molecular structure determination by electron microscopy of unstained crystalline specimens. *J. Mol. Biol.* **94:425-440.**

Unwin, P. N. T. and C. Taddei (1977) Packing of ribosomes in crystals from the lizard *Lacerta sicula*. *J. Mol. Biol.* **114:491-506.**

van Heel, M., G. Harauz, and E. V. Orlova (1996) A new generation of the IMAGIC image processing system. *J. Struct. Biol.* **116:17-24.**